IMMUNOLOGY

AMPK-dependent Parkin activation suppresses macrophage antigen presentation to promote tumor progression

Xinyu Wang[1,2]*†, Yiyi Li[1]†, Yan Li[1]†, Xiumei Wang[1,2], Hongrui Song[1], Yingzhao Wang[3], Chunliu Huang[4], Chengzhou Mao[5], Lixiang Wang[1,2], Cheng Zhong[1], Di Yu[6,7], Zijin Xia[1], Yongyi Feng[1], Jingjing Duan[8], Yujia Liu[1], Juanjuan Ou[9,10,11], Congzhou Luo[1], Wenhao Mai[1], Hai Hong[1,12], Weibin Cai[13,14], Limin Zheng[15], Jean-François Trempe[16], Edward A. Fon[17], Jing Liao[18]*, Wei Yi[19]*, Jun Chen[1,2,12,13]*

The constrained cross-talk between myeloid cells and T cells in the tumor immune microenvironment (TIME) restricts cancer immunotherapy efficacy, whereas the underlying mechanism remains elusive. Parkin, an E3 ubiquitin ligase renowned for mitochondrial quality control, has emerged as a regulator of immune response. Here, we show that both systemic and macrophage-specific ablations of Parkin in mice lead to attenuated tumor progression and prolonged mouse survival. By single-cell RNA-seq and flow cytometry, we demonstrate that Parkin deficiency reshapes the TIME through activating both innate and adaptive immunities to control tumor progression and recurrence. Mechanistically, Parkin activation by AMP-activated protein kinase rather than PTEN-induced kinase 1 mediated major histocompatibility complex I down-regulation on macrophages via Autophagy related 5–dependent autophagy. Furthermore, Parkin deletion synergizes with immune checkpoint blockade treatment and *Park2*$^{-/-}$ signature aids in predicting the prognosis of patients with solid tumor. Our findings uncover Parkin's involvement in suppressing macrophage antigen presentation for coordinating the cross-talk between macrophages and T cells.

INTRODUCTION

Cancer immunotherapy has revolutionized the paradigms of conventional therapies. Despite durable curative effects achieved in immune checkpoint blockade (ICB) treatment for certain malignancies (*1*–*4*), few patients with solid tumor benefit from it due to side effect, poor efficacy, and high recurrence (*5*, *6*). Multidimensional profiling on the tumor immune microenvironment (TIME) of patients receiving ICB treatment through transcriptomic and proteomic analyses has revealed that exhausted T cells and immunosuppressive myeloid cells in the TIME largely account for patients' low responsiveness to immunotherapies (*7*–*10*).

Growing evidences support that the cross-talk between myeloid cells and T cells is crucial for tumor immunosurveillance and immune escape in the TIME (*11*). As the largest population of myeloid cells, tumor-associated macrophages (TAMs) have been reported to capture and present tumor antigens to T cells, accompanied by the expression of soluble factors and costimulatory signals (*12*, *13*). However, TAMs in solid tumors usually exhibit immunosuppressive features. On one hand, TAMs are endowed with high expression levels of immune checkpoints [e.g., Programmed Death-Ligand 1 (PD-L1) and B7 homolog 4 (B7-H4)], chemokines and cytokines [e.g., C-C motif chemokine ligand 2 (CCL2), interleukin-6 (IL-6), IL-10, and transforming growth factor–β], and immunosuppressive molecules (e.g., arginine 1 and inducible nitric oxide synthase) (*14*, *15*). On the other hand, immunosuppressive TAMs reportedly form an "infiltration-rejection" tumor microenvironment due to their abundant infiltration, which severely attenuates the activation of tumor-specific T cells and the efficacy of immunotherapies (*16*, *17*). Hence, there persists a compelling need to find the mechanisms that link innate immunity to adaptive immunity, which regulate tumor immune escape.

PARK2 (encoding Parkin), whose mutations are the most frequent causes of recessive Parkinson's disease (PD), encodes a structurally autoinhibited E3 ubiquitin ligase (*18*, *19*). It is well established

---

[1] Department of Immunology and Microbiology, Zhongshan School of Medicine, Sun Yat-sen University, Guangzhou, China. [2] Jinfeng Laboratory, Chongqing, China. [3] Department of Gastrointestinal Surgery, The First Affiliated Hospital, Sun Yat-sen University, Guangzhou, China. [4] Nasopharyngeal Carcinoma Center, The Fifth Affiliated Hospital, Zhongshan School of Medicine, Sun Yat-sen University, Zhuhai, China. [5] Department of Anatomy and Histology, Shenzhen University Medical School, Shenzhen, China. [6] Frazer Institute, Faculty of Medicine, University of Queensland, Brisbane, QLD, Australia. [7] Ian Frazer Centre for Children's Immunotherapy Research, Child Health Research Centre, Faculty of Medicine, University of Queensland, Brisbane, QLD, Australia. [8] Department of Anatomy and Neurobiology, Zhongshan School of Medicine, Sun Yat-sen University, Guangzhou, China. [9] Yu-Yue Pathology Research Center, Chongqing, China. [10] Centre for Translational Research in Cancer, Sichuan Cancer Hospital & Institute, University of Electronic Science and Technology of China, No. 55 South Renmin Road, Third Inpatient Building, Chengdu, China. [11] Department of Oncology, Fuling Central Hospital of Chongqing City, Chongqing, China. [12] Key Laboratory of Tropical Disease Control of the Ministry of Education, Sun Yat-sen University, Guangzhou, China. [13] Guangdong Engineering & Technology Research Center for Disease-Model Animals, Laboratory Animal Center, Zhongshan School of Medicine, Sun Yat-sen University, Guangzhou, China. [14] Department of Biochemistry, Zhongshan School of Medicine, Sun Yat-sen University, Guangzhou, China. [15] Ministry of Education Key Laboratory of Gene Function and Regulation, State Key Laboratory of Biocontrol, School of Life Sciences, Sun Yat-sen University, Guangzhou, China. [16] Department of Pharmacology & Therapeutics and Centre de Recherche en Biologie Structurale, McGill University, Montréal, Canada. [17] McGill Parkinson Program, Neurodegenerative Diseases Group, Department of Neurology and Neurosurgery, Montreal Neurological Institute, McGill University, Montreal, Canada. [18] GMU-GIBH Joint School of Life Sciences, Guangdong-Hong Kong-Macau Joint Laboratory for Cell Fate Regulation and Diseases, Guangzhou Medical University, Guangzhou, China. [19] State Key Laboratory of Ophthalmology, Guangdong Provincial Key Laboratory of Ophthalmology and Visual Science, Zhongshan Ophthalmic Center, Sun Yat-Sen University, Guangzhou, China.
*Corresponding author. Email: wangxy775@mail.sysu.edu.cn (X.W.); liaojing@gzhmu.edu.cn (J.L.); yiwei@gzzoc.com (W.Y.); chenjun23@mail.sysu.edu.cn (J.C.)
†These authors contributed equally to this work.

that Parkin can be phosphorylated by PTEN-induced kinase 1 (PINK1) and recruited to mitochondria to ubiquitinate mitochondrial proteins, which ultimately removes damaged mitochondrial components by mitophagy (*20*, *21*). Beyond its vital role in mitochondrial quality control for cellular fitness, emerging research highlights Parkin's involvement in inflammation: (i) Patients with Parkin mutations and *Park2*$^{-/-}$ mice show elevated inflammatory factors such as IL-6 and tumor necrosis factor–α (TNF-α) (*22*, *23*); (ii) AMP-activated protein kinase (AMPK), which senses cellular adenosine 5′-diphosphate (ADP)/adenosine 5′-triphosphate (ATP) ratio, has been reported to activate Parkin independent of PINK1 and modulate inflammation (*24*, *25*); and (iii) Parkin purportedly inhibits stimulator of interferon (IFN) genes–induced inflammation and mitochondrial antigen presentation (*23*, *26*), suggesting that it orchestrates both innate and adaptive immunities under inflammatory conditions. In terms of tumorigenesis, Parkin has been characterized as a potential tumor suppressor, with frequently diminished expression and mutations in various tumors (*24*, *27*–*29*). Considering that the immunosuppressive milieu of TIME is accompanied by the fluctuations in ATP production, mitochondrial status, and complex inflammatory stimulation (*30*–*32*), it is intriguing to hypothesize that Parkin might regulate immune cell–mediated immunity in this context. Thus, whether and how Parkin modulates immune cells during tumor progression would be particularly attractive issues.

Here, we highlight Parkin as a negative immune regulator, which restrains the cross-talk between macrophages and T cells to underpin tumor immune evasion. Through various in vivo murine tumor progression models, we found that both systemic Parkin deficiency and macrophage-specific ablation of Parkin could inhibit the progression of multiple cancers. Single-cell transcriptomic and flow cytometry analyses profiled distinct antitumor macrophage and effector T cell subsets in the TIME of *Park2*$^{-/-}$ mice, which were further validated by adoptive transfer assays. Subsequent functional experiments showed that Parkin deficiency facilitates both innate and adaptive immune responses to remodulate the TIME and control tumor development and relapse. Mechanistically, Parkin suppresses major histocompatibility complex I (MHC-I) expression on TAMs through an unconventional AMPK-dependent pathway via the Autophagy related 5 (ATG5)–dependent autophagy activity, which was further validated by mice with conditional ATG5 knockout (KO) in macrophages. We found that *Park2*$^{-/-}$ signature is associated with improved prognosis in patients with solid tumor and targeting Parkin sensitizes ICB treatment, reinforcing Parkin as a promising target for cancer immunotherapy.

RESULTS

Parkin-deficient mice are resistant to tumor progression

To determine Parkin's impact in regulating antitumor immunity, we used a gene-deficient mouse strain lacking *Park2* to establish subcutaneous tumor models. *Park2*$^{-/-}$ (Parkin deficiency) mice showed stronger resistance to tumor progression than wild-type (WT) littermates in a syngeneic colon carcinoma MC38 model, in terms of tumor volume (Fig. 1A and fig. S1, A and B), tumor weight (fig. S1C), and survival (Fig. 1B). Similar results were observed when mice were inoculated with Hepa1-6 hepatocellular carcinoma cells (Fig. 1, C and D, and fig. S1D), CT2A glioma tumor cells (fig. S1, E and F), or E0771 breast cancer cells (fig. S1G), suggesting that Parkin-deficient mice exhibit resistance to the development of multiple subcutaneous solid tumors.

In vivo liver metastasis model of colon carcinoma also showed that Parkin deficiency extended mouse survival (fig. S1H). We then established orthotopic solid tumor models to verify the effects of Parkin deficiency on tumor development more physiologically. Orthotopic injection of Hepa1-6 cells into liver capsules led to favorable survival in *Park2*$^{-/-}$ mice compared with WT mice (Fig. 1E). The livers of tumor-inoculated WT mice contained tumors with larger quantities and volumes compared with those of *Park2*$^{-/-}$ mice, which had only small tumors and even tended to be normal (Fig. 1F and fig. S2A). Hematoxylin and eosin (H&E)–stained liver sections from *Park2*$^{-/-}$ mice revealed less lesions, confirmed by pale nuclei and pink cytoplasm (fig. S2, B and C). In parallel, in a murine glioma model, Parkin deficiency markedly impeded intracranial tumor growth and improved mouse survival (Fig. 1G), in line with the H&E staining that Parkin deficiency alleviated intracranial tumor load (Fig. 1H and fig. S2D). Collectively, these results indicate that loss of Parkin in mice prohibits the progression of multiple cancers.

T cells are essential for the superior antitumor effects in *Park2*$^{-/-}$ mice

To investigate the mechanisms responsible for Parkin deletion–mediated antitumor effects, we performed single-cell transcriptome sequencing [single-cell RNA sequencing (scRNA-seq)] on tumor-infiltrating CD45^{+} cells sorted from MC38 tumors in WT or *Park2*$^{-/-}$ mice. A total of 40,091 immune cells were obtained and partitioned into eight immune cell subsets (fig. S3A), which overlapped between *Park2*$^{-/-}$ and WT mice in the *t*-distributed stochastic neighbor embedding (t-SNE) plot (Fig. 1I). The TIME of *Park2*$^{-/-}$ mice was significantly distinct, with the increased proportions of natural killer (NK) cells, T cells, monocytes, granulocytes, and macrophages, and the decreased proportions of B cells and mast cells compared with that of WT mice (Fig. 1J and fig. S3B). Concordantly, the significantly increased proportions of the tumor-infiltrating T cells (TILs) in the TIME of *Park2*$^{-/-}$ mice were confirmed by flow cytometry (Fig. 1K and fig. S4A), while the proportions of other immune cell subsets remained similar between WT and KO mice (fig. S4, B to H).

As the ultimate effector cells of antitumor immunity, CD4^{+} and CD8^{+} T cells directly recognize and kill tumor cells, thus controlling tumor progression (*33*). Notably, both proportions of CD8^{+} and CD4^{+} T cells were significantly up-regulated in the TIME of *Park2*$^{-/-}$ mice (Fig. 1K), consistent with immunohistochemical staining of CD8 (fig. S4, I and J) and CD4 (fig. S4, K and L) in tumor sections. We also observed significantly up-regulated IL-2 and IFN-γ in tumor interstitial fluids of *Park2*$^{-/-}$ mice (Fig. 1, L and M), suggesting enhanced effector functions of T cells in the TIME of *Park2*$^{-/-}$ mice. We next set out to determine the contribution of T cells to Parkin deficiency–induced tumor regression. Depleting CD8^{+} T cells completely abrogated the superior tumor suppression in *Park2*$^{-/-}$ tumor–inoculated mice (Fig. 1, N and O), while deletion of CD4^{+} T cells partially rescued the decrease in tumor burden of *Park2*$^{-/-}$ mice (Fig. 1, N and P). Collectively, these data indicate that T cells are necessary for Parkin deficiency–mediated antitumor immunity.

Parkin deficiency indirectly activates TILs

To further probe the functional status of TILs, we clustered the T cell population and obtained 13 subclusters in the scRNA-seq data (Fig. 2A and fig. S5A). We found that the percentages of early activated CD8^{+}

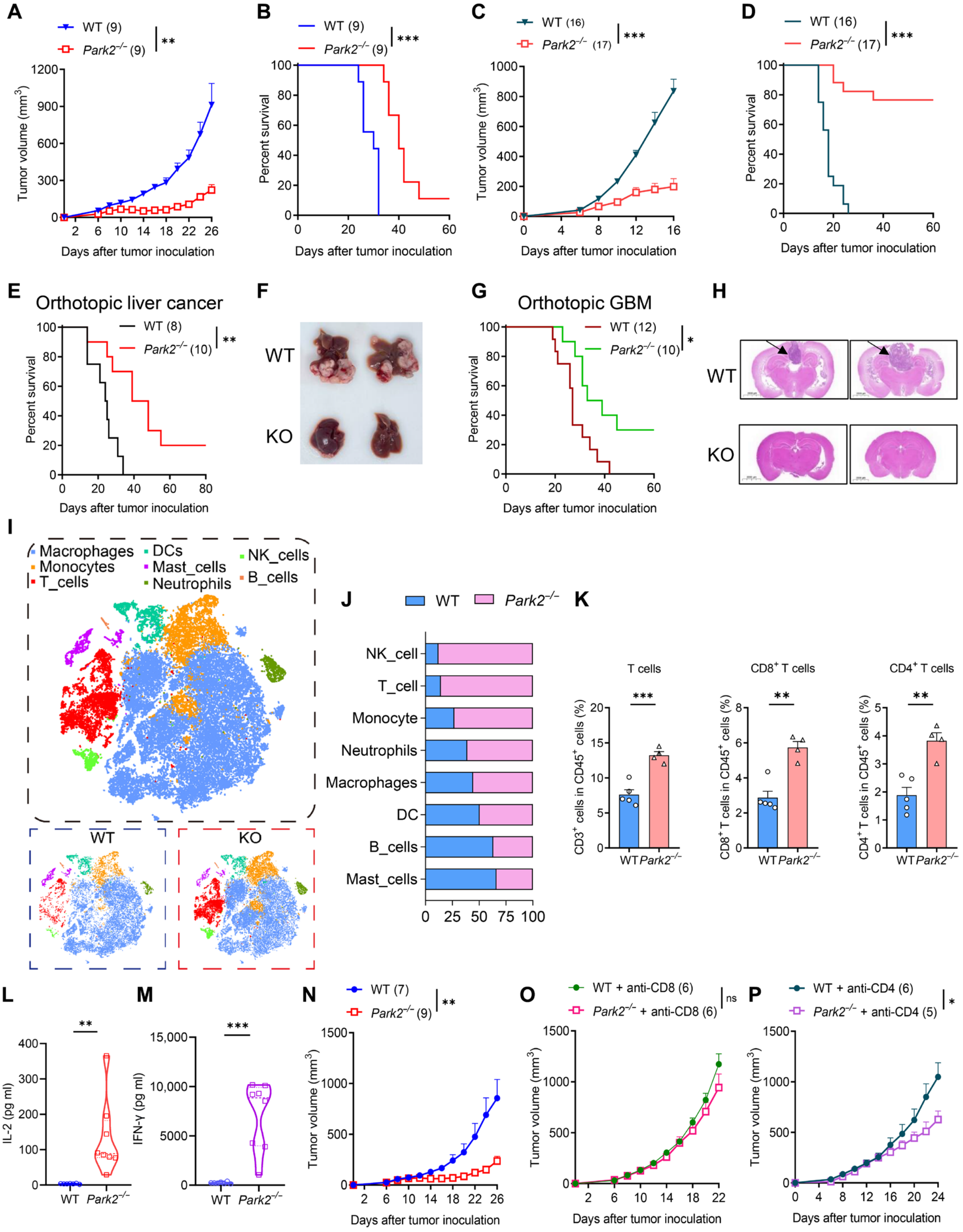

Fig. 1. Loss of Parkin in mice leads to reduced tumor burden in multiple cancers. (**A** and **B**) Tumor volume (A) and survival (B) of WT ($n = 9$) and *Park2*$^{-/-}$ ($n = 9$) mice bearing subcutaneous MC38 tumors. (**C** and **D**) Tumor volume (C) and survival (D) of WT ($n = 16$) and *Park2*$^{-/-}$ ($n = 17$) mice bearing subcutaneous Hepa1-6 tumors. (**E**) Survival analysis of WT ($n = 8$) and *Park2*$^{-/-}$ ($n = 10$) mice in an in situ model of hepatocellular carcinoma. (**F**) Representative images of hepatocellular carcinoma tumors. (**G**) Plot showing the overall survival (OS) of WT ($n = 12$) and *Park2*$^{-/-}$ ($n = 10$) mice intracranially inoculated with CT2A glioma cells. GBM, glioblastoma multiforme. (**H**) Representative histology of murine brains with intracranial tumors (tumor indicated by arrows). Images are representative of at least three images for one indicated animal. Scale bars, 2 cm. (**I**) *t*-distributed stochastic neighbor embedding (t-SNE) plot of 40,091 cells from WT or *Park2*$^{-/-}$ mice bearing MC38 tumors (pooled cells of two mice per group) analyzed by single-cell RNA sequencing (scRNA-seq). DCs, dendritic cells. (**J**) Proportions of major cell types in (I). (**K**) Percentages of T cells, CD8$^+$ T cells, and CD4$^+$ T cells in subcutaneous MC38 tumors in WT ($n = 5$) or *Park2*$^{-/-}$ ($n = 4$) mice. (**L** and **M**) IL-2 (L) and IFN-γ (M) in tumor interstitial fluids of WT ($n = 7$) and *Park2*$^{-/-}$ ($n = 8$) mice. (**N** to **P**) Tumor volumes of WT and *Park2*$^{-/-}$ MC38–bearing mice treated with (N) phosphate-buffered saline (PBS) and (O) anti-CD4 and (P) anti-CD8 antibodies. The numbers of mice are indicated. The results are depicted as the means ± SEM, $^*P < 0.05$, $^{**}P < 0.01$, and $^{***}P < 0.001$. ns, not significant.

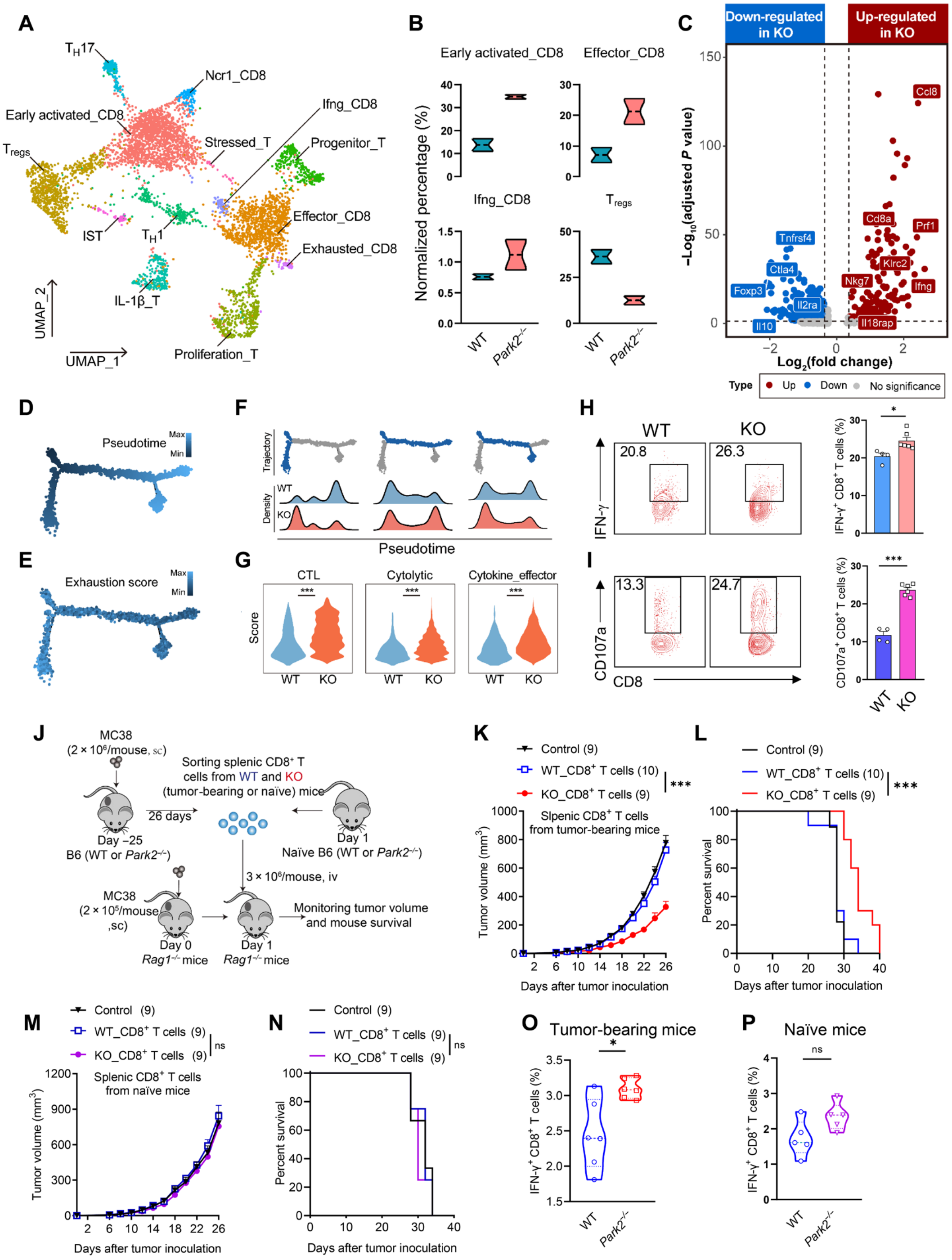

Fig. 2. Parkin deficiency leads to greater antitumor activity of TILs. (**A**) Annotated Uniform Manifold Approximation and Projection (UMAP) plot of T cells from tumors in WT and *Park2*$^{-/-}$ mice. T$_H$1, T helper cell 1; T$_H$17, T helper cell 17; IST, Interferon-response CD4$^+$ T cell. (**B**) Percentages of early activated_CD8, effector_CD8, Ifng_CD8, and T$_{regs}$ in WT and *Park2*$^{-/-}$ mice. (**C**) Volcano plot of differentially expressed genes (edgeR) of T cells from *Park2*$^{-/-}$ and WT mice (thresholds: at least 1.2 fold change, adjusted $P < 0.05$). (**D**) Trajectory analysis of T cells in WT and *Park2*$^{-/-}$ mice. (**E**) Expression of genes and a signature associated with T cell exhaustion differ in the three trajectory branches. (**F**) Relative proportions of T cells from WT and *Park2*$^{-/-}$ mice in different trajectory branches. (**G**) Enriched signatures of cytotoxic, cytolytic, and cytokine effector CD8$^+$ T cells from WT and *Park2*$^{-/-}$ mice. (**H** and **I**) Expression levels of IFN-γ (H) and CD107a (I) in TILs by fluorescence-activated cell sorting (FACS) analysis. T cells were isolated from MC38 tumors in WT ($n = 4$) or *Park2*$^{-/-}$ ($n = 6$) mice and stimulated with phorbol 12-myristate 13-acetate and ionomycin. (**J**) Experiment design. sc, subcutaneously; iv, intravenously. (**K** and **L**) Subcutaneous tumor volume (K) and OS (L) of *Rag1*$^{-/-}$ mice inoculated with MC38 cells and transplanted with WT or *Park2*$^{-/-}$ splenic CD8$^+$ T cells from tumor-bearing mice. The numbers of mice are indicated. (**M** and **N**) Subcutaneous tumor volume (M) and OS (N) of *Rag1*$^{-/-}$ mice inoculated with MC38 cells and transplanted with WT or *Park2*$^{-/-}$ splenic CD8$^+$ T cells from naïve mice. The numbers of mice are indicated. (**O** and **P**) Expression levels of the IFN-γ in splenic CD8$^+$ T cells from tumor-bearing (O) or naïve mice (P) ($n = 6$ per group). The results are depicted as the means ± SEM, $^*P < 0.05$ and $^{***}P < 0.001$.

T cells (CCL8^{hi}), effector CD8$^+$ T cells [NCR^{hi} (Natural Cytotoxicity Triggering Receptor 1) and NKG7^{hi} (Natural Killer Cell Granule Protein 7)], and IFN-γ$^+$ CD8$^+$ T cells were significantly increased, while the percentage of regulatory T cells (T$_{regs}$) was significantly decreased in the *Park2*$^{-/-}$ group (Fig. 2B). We also found abundant differentially expressed genes of T cells between WT and *Park2*$^{-/-}$ groups. Genes related to T cell recruitment, activation, and tumor killing, including *Ccl8*, *CD8a*, *Prf1*, *Klrc2*, *Nkg7*, *Ifng*, and *Il18rap*, were significantly up-regulated in the *Park2*$^{-/-}$ group. In contrast, genes related to T$_{reg}$ differentiation, recruitment, and immune suppression, such as *Tnfrsf4*, *Ctla4*, *Foxp3*, *Il2a*, and *Il10*, were significantly down-regulated in the *Park2*$^{-/-}$ group (Fig. 2C), substantiating a more tumoricidal phenotype. To further characterize the evolution and activation status of T cells, we performed trajectory analysis (Fig. 2D and fig. S5, B and C) coupled with exhaustion and inhibitory scoring (Fig. 2E and fig. S5D) on TILs. We found that T cells diverged into three developmental trajectories (left, upper, and upper-middle-lower) (Fig. 2F). With the progression of the pseudotemporal, on both left and upper-middle-lower trajectories, the proportion of T cells in the KO group gradually decreased, accompanied by increasing trends of exhaustion and inhibition scores; while on the upper pathway, the proportion of T cells in the KO group gradually increased, albeit to no significant increase in the exhaustion and inhibition scores. We also observed markedly enriched cytotoxic, cytolytic, and cytokine effector signatures of tumor-infiltrating CD8$^+$ T cells in the *Park2*$^{-/-}$ group compared with WT group (Fig. 2G). In parallel, we examined the expression levels of IFN-γ, CD107a, granzyme B, and TNF-α in the in vitro reactivated TILs sorted from WT or *Park2*$^{-/-}$ mice and observed marked elevation in both tumor-infiltrating CD8$^+$ (Fig. 2, H and I, and fig. S6, A and B) and CD4$^+$ T cells (fig. S6, C to F) from *Park2*$^{-/-}$ mice. Collectively, Parkin deficiency could reshape TILs into an enhanced activation and effector phenotype at transcriptional and protein levels.

We then performed CD8$^+$ T cell adoptive transfer assays to verify the in vivo effects of superior activated T cells in Parkin-deficient mice (Fig. 2J). Transfer of splenic CD8$^+$ T cells from tumor-bearing *Park2*$^{-/-}$ mice into MC38-inoculated *Rag1*$^{-/-}$ mice significantly attenuated tumor growth and prolonged survival (Fig. 2, K and L), prompting us to explore whether Parkin directly regulates naïve T cells for their enhanced activation in tumors. To address this, we transferred splenic CD8$^+$ T cells from naïve WT and *Park2*$^{-/-}$ mice into MC38-inoculated *Rag1*$^{-/-}$ mice but observed no significant difference in tumor progression of recipient mice (Fig. 2, M and N). We also observed comparable expression levels of T cell activation molecules, CD25, CD44, CD62L, CD69, and PD-1 between splenic T cells sorted from naïve WT and *Park2*$^{-/-}$ mice (fig. S6, G and H), indicating that Parkin deficiency is likely to influence T cell activation via T cell–extrinsic effects. Notably, we noticed that splenic CD8$^+$ T cells from tumor-inoculated *Park2*$^{-/-}$ mice (Fig. 2O) rather than naïve *Park2*$^{-/-}$ mice (Fig. 2P) secreted more IFN-γ in vitro than WT counterparts, in line with enhanced T cell activation in the TIME from *Park2*$^{-/-}$ mice (Figs. 1M and 2, G to I), implying that Parkin deficiency indirectly affects T cell–mediated antitumor effects by regulating some "intermediate" cells in the context of tumor challenging.

Macrophages are profoundly activated to cross-talk with T cells in Parkin-deficient TIME

The TIME is an equilibrium where various immune cell subsets interface with each other to regulate immunosurveillance or immune escape (*34*). As the largest population in the TIME, myeloid cells play pivotal roles in immunomodulation (*35*). Considering that Parkin might indirectly influence T cell activation through myeloid cells, we extracted myeloid cells from the scRNA-seq results and obtained five subpopulations, among which macrophages accounted for the largest proportion (Fig. 3A). Using the CellChat algorithm, we found that Parkin deficiency enhanced the intercellular communication between T cells (both CD4$^+$ and CD8$^+$ T cells) and myeloid cells (fig. S7, A and B), with macrophages consistently being the strongest communication counterparts with T cells (Fig. 3, B and C, and fig. S7, C and D).

Given that Parkin might regulate antitumor effects of T cells via macrophages, we then asked whether *Park2*$^{-/-}$ TAMs acquire a distinctive antitumor phenotype. Differential expression gene (DEG) analysis showed that *Park2*$^{-/-}$ TAMs significantly up-regulated genes in antigen presentation (e.g., *H2-K1*), proinflammatory polarization (e.g., *Il1*β and *Tnf*), and chemokines (e.g., *Ccl4*, *Ccl5*, and *Ccl8*) and down-regulated genes in protumor polarization (e.g., *Mgl1* and *Mrc1*)–related pathways (Fig. 3D). When macrophages were depleted by anti–colony-stimulating factor 1 receptor (anti-CSF1R) antibodies, the difference in tumor volume (Fig. 3E) and survival (fig. S7E) between WT and *Park2*$^{-/-}$ tumor–bearing mice disappeared. To probe whether Parkin expressed in macrophages induces tumor progression, we bred *Park2*$^{fl/fl}$-Lyz-Cre$^{+/-}$ mice whose *Park2* was conditionally KO in macrophages and determined low Parkin's expression levels in macrophages (fig. S7F). In the MC38 model, specific deletion of Parkin in macrophages impeded tumor growth (Fig. 3F) and tumor weight (fig. S7, G and H) and facilitated T cell infiltration in the TIME (Fig. 3G and fig. S7, I and J), which provides a strong support for our previous findings in *Park2*$^{-/-}$ mice (Fig. 1, A, B, and K, and fig. S1, A to C). Enhanced antitumor effects of *Park2*$^{-/-}$ macrophages in vivo were also confirmed by an adoptive transfer assay (Fig. 3H). We found that the transfer of *Park2*$^{-/-}$ bone marrow–derived macrophages (BMDMs) from naïve WT mice into tumor-inoculated WT mice significantly inhibited tumor growth (Fig. 3I) and prolonged survival (fig. S7K) in recipient mice, suggesting that *Park2*$^{-/-}$ macrophages are critical for the enhanced antitumor activity. These data collectively illustrate that Parkin expressed in macrophages induces tumor progression and targeting Parkin markedly impedes cancer progression.

We next sought to characterize the interaction between TAMs and T cells in the TIME of *Park2*$^{-/-}$ mice. First, *Park2*$^{-/-}$ TAMs scored significantly higher than WT TAMs in these signatures as inflammation, costimulation, antigen presentation, and proinflammatory polarization (Fig. 3J). Second, Reactome pathway enrichment analysis of *Park2*$^{-/-}$ TAMs showed up-regulated pathways including innate immune system and adaptive immune response (fig. S8A), indicating that *Park2*$^{-/-}$ TAMs are prone to an activated state and favorable to reinvigorate adaptive immune response. Last, intercellular ligand–receptor analysis showed that Parkin deficiency enhanced the interaction between macrophages and T cells through up-regulating costimulatory, antigen-presenting, and adhesion-related surface molecules (Fig. 3K). In addition, we focused on the

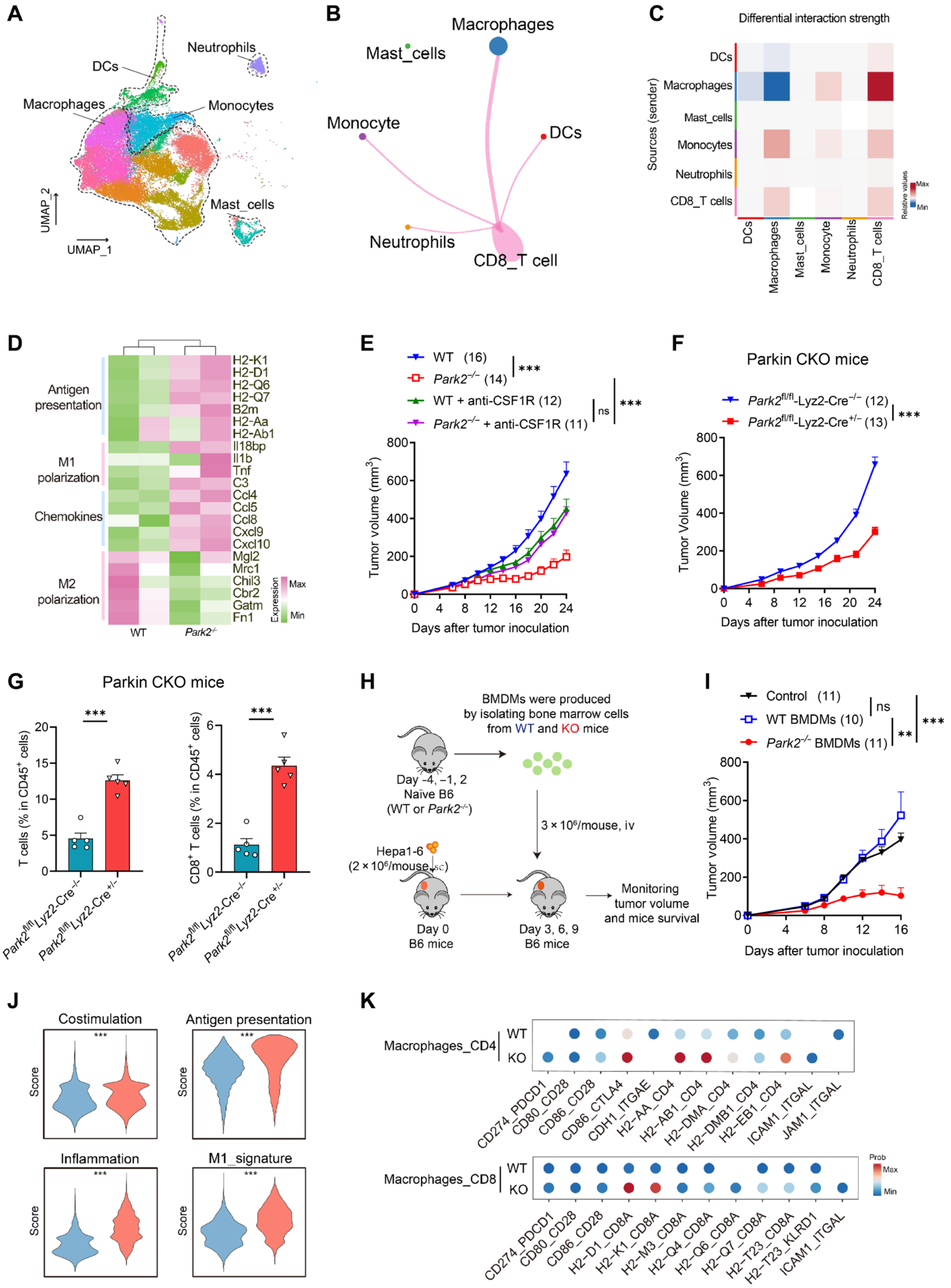

Fig. 3. Parkin deficiency enhances macrophage function and T cell activation. (**A**) Annotated UMAP plot showing scRNA-seq analysis of myeloid cells from tumors in WT and *Park2*$^{-/-}$ mice. (**B** and **C**) Differential strength of interactions between CD8^{+} T cells and myeloid cells in WT and *Park2*$^{-/-}$ mice. (**D**) Heatmap of the expression levels of selected genes in TAMs of WT and *Park2*$^{-/-}$ mice bearing MC38 tumors in scRNA-seq dataset. (**E**) Tumor volume of WT and *Park2*$^{-/-}$ mice treated with anti–colony-stimulating factor 1 receptor (anti-CSF1R) antibodies or left untreated after inoculation of MC38 cells. The numbers of mice are indicated. (**F**) Tumor volume of control (Ctrl; $n = 12$) and *Park2*$^{fl/fl}$-Lyz2-Cre$^{+/-}$ ($n = 13$) mice bearing subcutaneous MC38 tumors. CKO, conditional KO. (**G**) Percentages of T cells, CD8^{+} T cells in subcutaneous MC38 tumors in control ($n = 5$), or *Park2*$^{fl/fl}$-Lyz2-Cre$^{+/-}$ ($n = 5$) mice. (**H**) Experiment design. (**I**) Tumor volume of WT mice inoculated with Hepa1-6 cells and transplanted with WT or *Park2*$^{-/-}$ bone marrow–derived macrophages (BMDMs). The numbers of mice are indicated. (**J**) Transcripts from macrophages in tumors from WT and *Park2*$^{-/-}$ mice in scRNA-seq dataset were assessed for enrichment of signatures of costimulation, antigen presentation, inflammation, and M1-type macrophages. (**K**) Bubble heatmap showing the interactions of selected ligand-receptor pairs between TAMs from WT or *Park2*$^{-/-}$ mice and T cell subpopulations based on scRNA-seq analysis of the MC38 model. The results are depicted as the means ± SEM, $^{**}P < 0.01$ and $^{***}P < 0.001$.

effector_CD8$^+$ T cells and early activated_CD8$^+$ T cell subpopulations that were enriched in the KO group and analyzed their intercellular interactions with macrophages. We found that Parkin deficiency significantly enhanced their interactions, confirmed by up-regulated cytokine ligand receptors such as IFN-γ and type II IFN receptors, cell adhesion ligand receptors such as intercellular adhesion molecule–1 (ICAM1), and chemokine ligand receptors such as CXCL16 and CXCR6 (fig. S8B). Collectively, these results suggest that Parkin deficiency profoundly reprograms macrophages to reinvigorate adaptive immunity.

Parkin deficiency facilitates macrophage antigen presentation to prime antigen-specific T cells

To investigate the mechanism by which Parkin regulates TAMs, we clustered the macrophage population in the scRNA-seq data and obtained 10 subpopulations (fig. S9A), which reportedly exhibit antitumor or protumor effects, respectively (*36*). The antitumor TAMs were classified into three subclusters (macro_CD80, macro_Ccl12, and macro_C1qc), among which the proportions of macro_CD80 and macro_C1qc clusters increased in the *Park2*$^{-/-}$ group (fig. S9B). We next analyzed the enriched pathways shared by these two clusters. Kyoto Encyclopedia of Genes and Genomes (KEGG) pathway enrichment analysis showed that the shared pathways were "TNF signaling pathway," "phagosome," "nuclear factor κB (NF-κB) signaling pathway," "cytokine-cytokine receptor interaction," and "antigen processing and presentation," with "antigen presentation"–related pathways being consistently enriched in Gene Ontology (GO) pathway enrichment analysis (Fig. 4A). Computation of immune enrichment scoring on macro_CD80 and macro_C1qc macrophage clusters revealed significantly increased proinflammatory and antigen presentation signatures and pathway-related gene expression in the *Park2*$^{-/-}$ group compared with WT group (Fig. 4, B to D).

As the critical sentinels of immune system, macrophages can phagocytose, process, and cross-present exogenous antigens to antigen-specific T cells in the context of MHC-I (*37*, *38*). Parkin deficiency hardly affects macrophage phagocytosis as WT or *Park2*$^{-/-}$ BMDMs phagocytosed tumor cells at comparable levels (fig. S10, A and B). In terms of cross-presentation, we found that the MHC-I signaling pathway network between macrophages and CD8$^+$ T cells was significantly up-regulated in the *Park2*$^{-/-}$ group (fig. S10C). Considering increased MHC-I expression on *Park2*$^{-/-}$ BMDMs when cocultured with MC38 and L1210 (fig. S10, D and E), we conducted in vitro antigen presentation experiments and found that ovalbumin (OVA)–impulsed *Park2*$^{-/-}$ BMDMs presented more SIINFEKL (fig. S10F) and displayed a significantly stronger ability to promote OT-I T cell proliferation than WT BMDMs (Fig. 4E). Similarly, we observed increased MHC-I expression on TAMs isolated from *Park2*$^{-/-}$ mice at protein levels (Fig. 4F) and stronger T cell priming ability of ex vivo isolated *Park2*$^{-/-}$ TAMs than those from WT mice (Fig. 4G), in line with the findings of the TAMs from *Park2*$^{fl/fl}$-Lyz2-Cre$^{+/-}$ mice (Fig. 4H and fig. S10G). Besides increased T cell priming, we found that these OT-I T cells primed by *Park2*$^{-/-}$ (Fig. 4I) or *Park2*$^{fl/fl}$-Lyz2-Cre$^{+/-}$ TAMs secreted more IFN-γ than the control group (Fig. 4J and fig. S10H), in line with elevated expression levels of IFN-γ production pathway–related genes in *Park2*$^{-/-}$ immune cells (Fig. 4K) and increased IFN-γ in *Park2*$^{-/-}$ tumor interstitial fluids (Fig. 1M). In vivo, IFN-γ is indispensable for Parkin deficiency–mediated antitumor effects, as IFN-γ blockade in the MC38 model almost completely abolished the difference in tumor growth between WT and *Park2*$^{-/-}$ mice (Fig. 4L).

Antigen-presenting cells loaded with tumor antigens could prime antigen-specific T cells for clone expansion, and afterward, the proliferated antigen-specific T cells used T cell receptors (TCRs) to recognize, kill tumors, and even sustain long-term immune memory (*39*). To address this, we performed TCR sequencing (TCR-seq) on TILs sorted from tumors of WT and *Park2*$^{-/-}$ mice. We observed an increased clonality along with a reduced diversity of TCRs from *Park2*$^{-/-}$ TILs (Fig. 4M and fig. S10, I and J), supporting that T cells primed by *Park2*$^{-/-}$ TAMs are prone to expand antigen-specific TCR clones. Moreover, immune enrichment scoring of scRNA-seq data showed that T cells from *Park2*$^{-/-}$ tumor–inoculated mice acquired an enhanced memory signature (Fig. 4, N and O). When we rechallenged fivefold numbers of tumor cells in the *Park2*$^{-/-}$ mice that had recovered after primary tumor inoculation, all the rechallenged tumors were markedly eradicated in *Park2*$^{-/-}$ convalescent mice (Fig. 4P). Together, these results indicate that Parkin influences the effector and memory functions of T cells through regulating macrophage antigen presentation.

AMPK-dependent activation of Parkin reduces MHC-I expression on macrophage surface via autophagy

Parkin is autoinhibited with barely E3 ligase catalytic activity. Canonically, Parkin can be phosphorylated at S65 site of the ubiquitin-like domain by PINK1, resulting in its activation and translocation to defective mitochondria for mitophagy (*20*, *21*). We therefore examined whether Parkin regulates macrophage antigen presentation through PINK1-dependent activation and mitophagy in a subcutaneous MC38 model. Unexpectedly, the tumor progression and survival in *Pink1*$^{-/-}$ mice were comparable with those in WT mice (Fig. 5, A and B), suggesting that Parkin regulates macrophage antigen presentation through a PINK1-independent mechanism. To investigate the molecular mechanism of Parkin in antigen presentation, we constructed macrophage cell lines by overexpressing a set of Parkin variants in Raw264.7 cells and examined their MHC-I expression levels on plasma membrane (fig. S11, A to C). First, we found that overexpressing full-length Parkin significantly down-regulated both the surface and total cellular levels of MHC-I on macrophages (Fig. 5, C to E), in agreement with our above findings that Parkin deficiency facilitates MHC-I expression (Fig. 4F and fig. S10, D and E). Meanwhile, overexpressing Parkin catalytic dead mutant C430S (akin to C431S in human) (*18*) barely affected MHC-I levels, indicating that Parkin suppressed antigen presentation through its ubiquitination activity (Fig. 5F). However, overexpressing Parkin mutant S65A, which blocks the phosphorylation and activation by PINK1, still significantly down-regulated MHC-I expression such as WT Parkin (Fig. 5F), consistent with the observation that PINK1 deficient mice failed to recapitulate Parkin deficiency–mediated antitumor effects in vivo (Fig. 5, A and B).

The AMPK/ULK1 (Unc-51 Like Autophagy Activating Kinase 1) axis has been reported to phosphorylate Parkin's Activation Critical Threshold domain (Parkin's ACT) domain at S108 site for its activation (*25*). We found that overexpressing Parkin mutant S108A rectified Parkin-induced MHC-I down-regulation (Fig. 5F), suggesting that the AMPK/ULK1 axis activates Parkin to decrease MHC-I expression. AMPK is rapidly activated following any stress that triggers a lowering of intracellular ADP/ATP ratio, which initiates ULK1 phosphorylation and the downstream components of

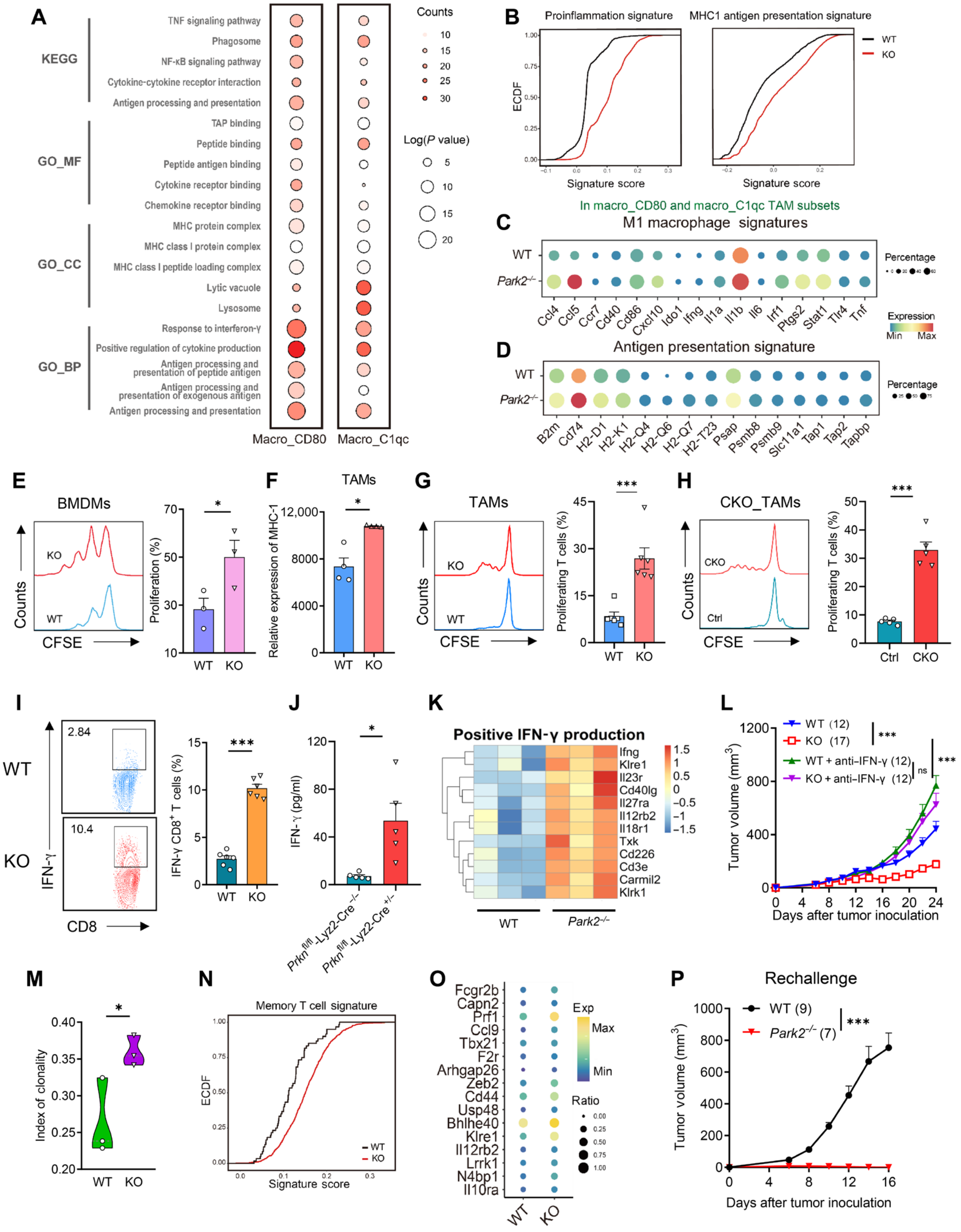

Fig. 4. Parkin suppresses antigen presentation of macrophages. (**A**) Enrichment analysis of up-regulated genes in *Park2*$^{-/-}$ macrophages from macro_CD80 and macro_C1qc macrophage subgroups. GO_BP, Gene Ontology: Biological process; GO_CC, Gene Ontology: Cellular component; GP_MF, Gene Ontology: Molecular function. TAP, TAP protein is a heterodimeric peptide transporter consisting of the subunits TAP1 and TAP2. (**B**) ECDF plots of enrichment score for proinflammation and MHC-I antigen presentation signatures in WT (black) or *Park2*$^{-/-}$ (red) macro_CD80 and macro_C1qc macrophages. (**C**) Dot plot of selected genes from M1 macrophage signatures. (**D**) Dot plot of selected genes from antigen presentation signature. (**E**) Representative images and proportions of OT-I T cells stimulated with BMDMs from ($n = 3$ per group). (**F**) MHC-I expression of TAMs in subcutaneous MC38 tumors ($n = 4$ per group). (**G** and **H**) Representative images and proportions of OT-I T cells stimulated with TAMs for 72 hours ($n = 3$ per group) (G) or control and *Park2*$^{fl/fl}$-Lyz2-Cre$^{+/-}$ mice ($n = 5$ per group) (H). (**I**) Representative images and proportions of IFN-γ^{+} OT-I T cells after cocultured with BMDMs ($n = 6$ per group). (**J**) Secreted IFN-γ of OT-I T cells after cocultured with TAMs for 72 hours ($n = 5$ per group). (**K**) Heatmap of the expression levels of genes related to IFN-γ production of in MC38 tumors from WT and *Park2*$^{-/-}$ mice in bulk RNA-seq dataset. (**L**) Tumor volume of WT and *Park2*$^{-/-}$ MC38–bearing mice with IFN-γ blockade. The numbers of mice are indicated. (**M**) Productive clonality in WT or *Park2*$^{-/-}$ TILs ($n = 3$ per group). (**N**) ECDF plot of enrichment score for memory T cell signature in WT (black) or *Park2*$^{-/-}$ (red) T cells. (**O**) Dot plot of selected genes in memory T cell signature. (**P**) Tumor growth of WT ($n = 9$) or tumor-free *Park2*$^{-/-}$ ($n = 7$) mice rechallenged with fivefold numbers of Hepa1-6 cells. The results are depicted as the means ± SEM, $^{*}P < 0.05$ and $^{***}P < 0.001$.

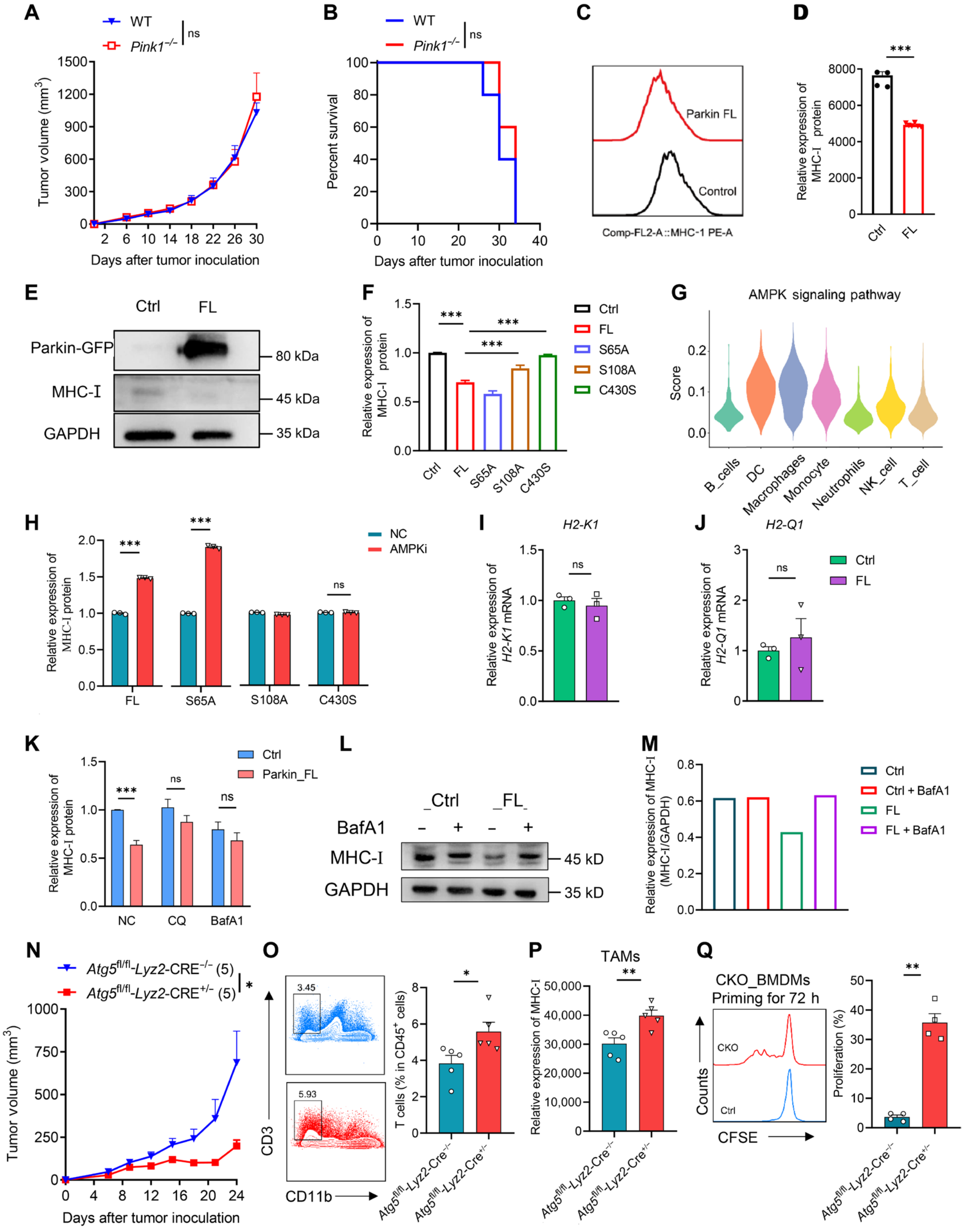

Fig. 5. AMPK-dependent Parkin activation suppresses MHC-I presentation via autophagy. (**A** and **B**) Tumor growth (A) and OS (B) of WT and $Pink1^{-/-}$ mice bearing subcutaneous MC38 tumors ($n = 5$ per group). (**C** and **D**) Representative image (C) and surface levels of MHC-I (D) on control and Parkin full-length Raw264.7 cells ($n = 6$ per group). Comp-FL2-A, Compensated Signal Fluorescence Channel 2 Area; PE-A, Phycoerythrin Area Parameter. (**E**) Total cellular levels of Parkin and MHC-I on control and Parkin full-length Raw264.7 cells. GAPDH, glyceraldehyde-3-phosphate dehydrogenase. (**F**) Surface levels of MHC-I on control, Parkin full-length, Parkin S65A, S108A, and C430S mutant Raw264.7 cells ($n = 9$ per group). (**G**) Expression and activity of the AMPK signaling in immune subpopulations. (**H**) Surface levels of MHC-I on Parkin full-length, Parkin S65A, S108A, and C430S mutant Raw264.7 cells treated without (NC) or with inhibitors of AMPK (AMPKi) ($n = 3$ per group). (**I** and **J**) mRNA expression levels of H2-K1 and H2-Q1 on control and Parkin full-length Raw264.7 cells ($n = 3$ per group). (**K**) Surface levels of MHC-I on control and Parkin full-length Raw264.7 cells treated without or with inhibitors of autophagy [CQ and bafilomycin A1 (BafA1)] ($n = 6$ per group). (**L** and **M**) Western blot of MHC-I expression in control and Parkin full-length Raw264.7 cells treated with BafA1. (**N**) Tumor growth of WT and $Atg5^{fl/fl}$-Lyz2-$Cre^{+/-}$ mice bearing subcutaneous MC38 tumors ($n = 5$ per group). (**O**) Representative image and percentages of T cells in MC38 tumors ($n = 5$ per group). (**P**) MHC-I expression of TAMs in MC38 tumors from control and $Atg5^{fl/fl}$-Lyz2-$Cre^{+/-}$ mice ($n = 5$ per group). (**Q**) Representative images and proportions of proliferating OT-I T cells stimulated with TAMs for 72 hours (h) ($n = 4$ per group). The results are depicted as the means ± SEM, $^{*}P < 0.05$, $^{**}P < 0.01$, and $^{***}P < 0.001$.

autophagy cascade (*40*, *41*). Considering the findings that the activation of autophagy promotes MHC-I internalization and restricts antigen presentation (*42*), we speculated whether AMPK/ULK1 activates Parkin to decrease MHC-I expression through elevated autophagy. Single-sample gene set enrichment analysis (ssGSEA) demonstrated that TAMs exhibited the strongest activity of AMPK pathway in the TIME (Fig. 5G). Further, applying AMPK inhibitor on the raw cells overexpressing Parkin S65A mutant rather than the S108A or C430S mutant enhanced the surface levels of MHC-I (Fig. 5H), confirming the AMPK-dependent Parkin activation in regulating antigen presentation. Overexpression of Parkin barely changed the mRNA expression level of MHC-I (H2-K1 and H2-Q1), suggesting that the decreased protein levels of MHC-I were independent of transcriptional regulation (Fig. 5, I and J). In contrast, the decreased surface levels of MHC-I induced by Parkin overexpression in Raw267.4 cells were rescued by autophagy inhibitors chloroquine (CQ) and bafilomycin A1 (BafA1) (Fig. 5K). Consistently, applying BafA1 substantially increased total cellular levels of MHC-I in raw cells overexpressing full-length Parkin but scarcely changed those in control cells (Fig. 5, L and M). Last, we use *Atg5*$^{fl/fl}$-Lyz2-Cre$^{+/-}$ mice whose *Atg5* is deleted in macrophages (fig. S12A) to examine whether specific deletion of autophagy in macrophage influences tumor progression and macrophage antigen presentation. In vivo MC38 model showed that specific deletion of Atg5 in macrophages impeded tumor growth (Fig. 5N and fig. S12B) and facilitated T cell infiltration in the TIME (Fig. 5O and fig. S12, C and D) and MHC-I expression on TAMs (Fig. 5P). Antigen presentation assays also showed significantly stronger T cell priming ability of *Atg5*$^{fl/fl}$-Lyz2-Cre$^{+/-}$ TAMs and BMDMs than the control group (Fig. 5Q and fig. S12E). Collectively, these findings suggest that AMPK-dependent Parkin activation suppresses MHC-I expression on macrophage surface via autophagy.

Parkin-associated signatures correlate with poor prognosis

Given the Parkin deficiency–mediated antitumor effects that we confirmed in preclinical tumor models, we next set out to assess the clinical relevance of *Park2* in ICB treatment. First, using ssGSEA algorithm, we found that the expression level of *Park2* was significantly inversely correlated with the abundance of activated CD8$^+$ T cells (Fig. 6A) and effector memory CD8$^+$ T cells (fig. S13A) in various solid tumors. Then, we stratified patients with metastatic urothelial cancer (mUC) from the IMvigor210CoreBiologies R package (26359337) based on responders and nonresponders receiving PD-L1 blockade and found that nonresponders had higher *Park2* expression than responders (Fig. 6B). Meanwhile, significant associations were shown between low expression of *Park2* and better overall survival in patients with mUC and progression-free survival in patients with melanoma receiving ICB therapies (fig. S13, B to D). Therefore, we wonder whether Parkin deficiency could improve the efficacy of ICB treatment in an MC38 model, which is responsive to anti–PD-L1 therapy. Anti–PD-L1 treatment indeed demonstrated better tumoricidal efficacy in *Park2*$^{-/-}$ mice than WT mice (Fig. 6C). Collectively, these results attest to the clinical relevance of Parkin deficiency in T cell infiltration and sensitivity to cancer immunotherapy.

As Parkin deficiency modulates macrophage antigen presentation and inflammatory response to facilitate T cell proliferation and activation, we suspected that *Park2*$^{-/-}$ signaling could be beneficial for predicting patients' prognosis in human tumors. To do so, we intersected genes up-regulated in macro_CD80 and macro_C1qc TAMs of the *Park2*$^{-/-}$ group to establish an overall *Park2*$^{-/-}$ activation signature (hereafter referred to as the *Park2*$^{-/-}$ signature) based on scRNA-seq data. This signature consists of genes directly and indirectly controlled by *Park2* in the transcriptional regulatory network of TAMs (fig. S13E). GO functional enrichment analysis showed that genes in the *Park2*$^{-/-}$ signature were significantly enriched in pathways including chemokine binding, antigen peptide binding, and immune response–related pathways (fig. S13F). We then applied the *Park2*$^{-/-}$ signature to 31 types of patients with tumor from The Cancer Genome Atlas (TCGA) dataset. A pan-cancer survival analysis showed that up-regulation of *Park2*$^{-/-}$ signature was associated with improved prognostic indicators overall survival (OS), dextran sulfate sodium (DSS), and progression free interval (PFI) in patients (Fig. 6, D to K), indicating that *Park2*$^{-/-}$ signature could serve as a biomarker for effectively predicting the prognosis for various patients with solid tumor. Overall, these results suggest that Parkin can be considered either a single target or a set of signature genes, providing perspectives for existing immunotherapies.

DISCUSSION

Parkin has long been portrayed as a neuroprotector, as its dysfunction is largely ascribed to neurodegeneration in patients with PD (*19*). Emerging evidences have implicated Parkin as a tumor suppressor regarding tumorigenesis (*24*, *27*–*29*) but whether Parkin regulates immune cell–intrinsic immunity in the TIME remains largely unresolved. Here, we find that Parkin negatively modulates antitumor immunity in the TIME, as Parkin deficiency reshapes the immunosuppressive TIME and prohibits tumor progression (Figs. 1 to 4). In this context, depletion of either *Park2*$^{-/-}$ CD8$^+$ T cells (Fig. 1, N and O) or macrophages (Fig. 3, E and F) abolishes Parkin deficiency–mediated tumor regression. Our data shed light on the essential role of macrophages in Parkin-mediated immune response, as demonstrated by superior antitumor effects of *Park2*$^{-/-}$ BMDMs (Fig. 3, H and I) rather than naïve *Park2*$^{-/-}$ splenic T cells (Fig. 2, M and N) in adoptive transfer assays. Although normalization of adaptive immunity has primarily been perceived as a fundamental strategy for immunotherapy (*43*, *44*), it would be of great importance to targeting innate immunity to reverse the immunosuppression of the TIME. Ongoing efforts have focused on equipping TAMs with effector functions, including direct phagocytosis, activation of inflammation, and professional antigen presentation (*45*, *46*). In our work, *Park2*$^{-/-}$ TAMs show enhanced inflammatory response and antigen presentation (Fig. 4, A to D) and further facilitate T cell priming, clonal expansion, and long-term memory (Fig. 4, E to G, I, and K to P), which were further validated in mice with macrophage-specific Parkin KO (Fig. 4, H and J, and fig. S10, F to H). Overall, the above data underscore the interplay between TAMs and T cells in shaping antitumor immunity.

Cancer and PD, two entirely different classes of disease, can converge on a single gene, *PARK2*. One possible reason is the modulation of inflammatory response, as patients with PD (*22*) and tumor inoculated–*Park2*$^{-/-}$ mice (Figs. 3J and 4C) show elevated inflammatory factors. Previous studies have demonstrated that kinases PINK1 and AMPK, which sense deleterious leakage of mitochondrial DNA and cellular ADP/ATP ratio, respectively, could activate Parkin to regulate inflammatory response (*20*, *21*, *23*–*25*), implying a Parkin-related activation cascade in regulating antitumor immunity.

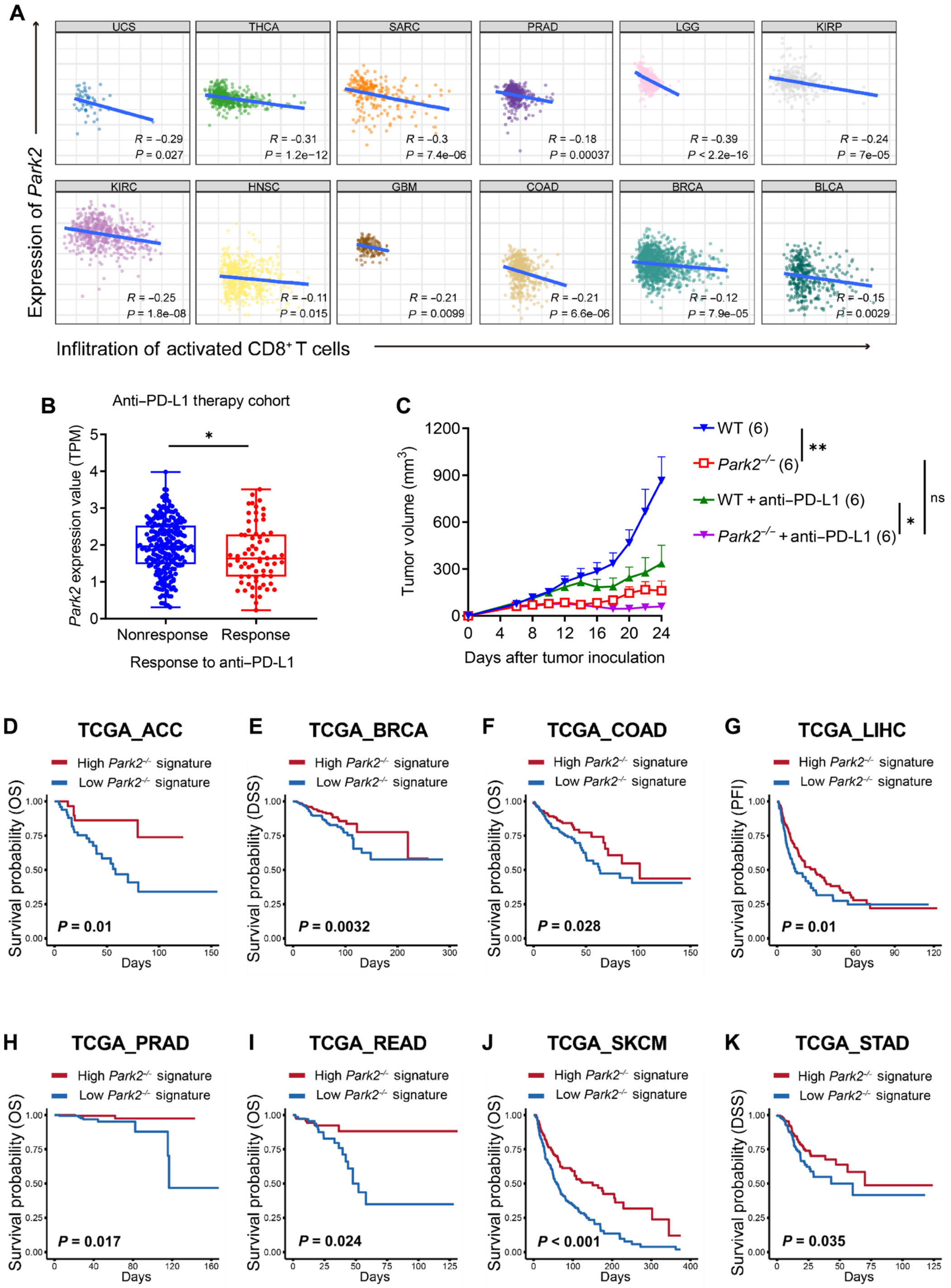

Fig. 6. The absence of Parkin enhances the efficacy of ICB therapy, and Parkin is a potential therapeutic target for cancer immunotherapy. (**A**) Correlation analysis between the expression of *Park2* and the infiltration of activated CD8$^+$ T cells in various tumors. UCS, Uterine carcinosarcoma; THCA, Thyroid carcinoma; SARC, Sarcoma; PRAD, Prostate Adenocarcinoma; LGG, Low-grade gliomas; KIRP, Kidney renal papillary cell carcinoma; KIRC, Kidney Renal Clear Cell Carcinoma; HNSC, Head and neck squamous cell carcinoma; GBM, Glioblastoma multiforme; COAD, Colon adenocarcinoma; BRCA, Breast Invasive Carcinoma; BLCA, Bladder Urothelial Carcinoma. (**B**) Expression of *Park2* in patients with mUC who received neoadjuvant anti–PD-1 therapies (GSE26359337). (**C**) Tumor volume of WT and *Park2*$^{-/-}$ MC38–bearing mice administered intraperitoneally with anti-mouse PD-L1 or left untreated on days 9, 12, 15, and 18. The numbers of mice are indicated. (**D** to **K**) Correlation of the *Park2*$^{-/-}$ signature score with overall survival (OS), dextran sulfate sodium (DSS), and progression free interval (PFI) in adenoid cystic carcinoma (ACC) (D), breast cancer (BRCA) (E), colon adenocarcinoma (COAD) (F), liver hepatocellular carcinoma (LIHC) (G), prostate adenocarcinoma (PRAD) (H), rectum adenocarcinoma (READ) (I), skin cutaneous melanoma (SKCM) (J), and stomach adenocarcinoma (STAD) (K). Low *Park2*$^{-/-}$ signature, blue curve; high *Park2*$^{-/-}$ signature, red curve. The results are depicted as the means ± SEM, *$P < 0.05$ and **$P < 0.01$.

Conventional PINK1/Parkin-mediated mitophagy seems to be negligible for immune cell activation in the TIME, as *Pink1*$^{-/-}$ mice exhibit no tumor inhibition effect such as *Park2*$^{-/-}$ mice (Fig. 5, A and B) and mutation of the key PINK1 phosphorylation site in Parkin does not affect Parkin's function in terms of MHC-I regulation (Fig. 5F). Instead, we demonstrate that the regulation of MHC-I by Parkin requires the activation of the AMPK/ULK1 axis in conjunction with the downstream autophagy components (Fig. 5, H to M), which were further validated in autophagy-deficient mice with a macrophage-specific manner (Fig. 5, N to Q).

Down-regulation of MHC-I expression has been reported to be kidnapped by tumor cells to avoid immunosurveillance (*47*). Excessive autophagy purportedly degrades ubiquitinated MHC-I in tumor cells via the autophagy cargo receptor NBR1, which, in turn, impairs T cell response and favors immune evasion of pancreatic cancer (*42*). Here, we find an unreported mechanism of Parkin in macrophages, which leverages AMPK activation and autophagy to regulate MHC-I surface expression, thereby broadening the role of AMPK/Parkin/autophagy axis beyond mitochondrial homeostasis. Meanwhile, MHC-I has been shown to be expressed at the surface of dopaminergic neurons in patients with PD, providing further support for the plausibility of MHC-I regulation in the development of PD (*48*). Thus, it would be interesting to characterize the direct substrates of AMPK-induced Parkin–mediated ubiquitination in regulating MHC-I, which could provide insight into understanding both Parkin-mediated tumor development and PD pathology.

Despite significant improvements made in ICB treatment, current immunotherapies urgently require promising targets and prognosis biomarkers (*49*). Here, our work provides important implications for improving current ICB treatment. We demonstrate that the expression level of *Park2* is negatively correlated with the infiltration of tumor-killing CD8^{+} T cells in tumor tissues (Fig. 6A and fig. S13A) and with the sensitivity of existing tumor immunotherapies (Fig. 6, B and C). In addition, we established a *Park2*$^{-/-}$ signature consisting of genes up-regulated in *Park2*$^{-/-}$ TAMs and, as a proof of concept, confirmed its efficacy as a biomarker for predicting prognosis for ICB treatment (Fig. 6, D to K). In light of in vivo antitumor effects of *Park2*$^{-/-}$ BMDMs (Fig. 3, H and I), targeting Parkin in chimeric antigen receptor macrophages (CAR-macrophages) holds promise for optimized cellular immunotherapy to overcome the limited infiltration of chimeric antigen receptor T cells into immunologically cold solid tumors (*50*). Collectively, Parkin acts as a negative immune regulator to favor tumor progression and could serve as a promising target or a signature gene set to improve current immunotherapies.

Overall, we demonstrate that targeting Parkin could not only enhance antigen presentation and inflammatory response of macrophages but also unleash the effector function of CD8^{+} T cells against solid tumors. Our findings provide a fresh perspective on targeting innate immunity to tailor adaptive immunity, thereby eliciting a systemic antitumor immune response for cancer immunotherapy.

MATERIALS AND METHODS

Mice

All mouse experiments were approved by the Institutional Animal Care and Use Committee of Sun Yat-sen University (approval number: SYSU-IACUC-2023-000800). *Park2*$^{-/-}$ (B6.129S4-*Prkn*$^{\mathrm{tm1Shn}}$/J) and *Pink1*$^{-/-}$ (B6.129S4-*Pink1*$^{\mathrm{tm1Shn}}$/J) mice were obtained from the Jackson Laboratory. WT (C57BL/6 J) and *Rag1*$^{-/-}$ mice were purchased from GemPharmatech Co. Ltd., Nanjing, Jiangsu, China. Prkn-flox mice (strain S-CKO-11411) were purchased from Cyagen. Atg5-flox mice were provided by Z. Li from Southern Medical University. Lyz2-Cre mice were purchased from Shulaibao (Wuhan) Biotechnology Co. Ltd. Both male and female mice were used in this study. The sex of mice was not considered a covariate factor. All mice used in this study were between 8 and 24 weeks of age and were housed under specific pathogen–free condition at the animal facility of the Laboratory Animal Center of Sun Yat-sen University.

Cell lines and cell culture

Murine colon adenocarcinoma MC38 (provided by R. Xu from Sun Yat-sen University Cancer Center), glioblastoma multiforme cancer cell line CT2A (provided by Q. Xie from West Lake University), hepatocellular carcinoma Hepa1-6, breast cancer cell line E0771 (provided by H. Zheng from Tsinghua University), fibroblast L929 cells (American Type Culture Collection), and macrophage cell line Raw264.7 (American Type Culture Collection) were cultured in Dulbecco's modified Eagle's medium containing 2 mM glutamine (Thermo Fisher Scientific) and were supplemented with 1% penicillin-streptomycin (Thermo Fisher Scientific) and 10% fetal bovine serum (FBS; TransGen Biotech). Cell lines were routinely tested for mycoplasma, and none of cell lines were positive in the reported experiments.

Mouse BMDMs were produced as described previously (*51*, *52*). Briefly, mouse bone marrow cells were cultured in the medium with 10% FBS, 1% penicillin-streptomycin, and 30% (v/v) L929 cell–conditioned medium as a source of macrophage CSF. On days 4 and 7, the medium was half replaced with fresh medium. After 7 days, mature BMDMs were pretreated with different compounds at corresponding conditions.

Subcutaneous tumor models

Tumor cells were digested into single cells by trypsin (Gibco) and washed three times with cold phosphate-buffered saline (PBS). A total of 2×10^{6} MC38, 2×10^{6} Hepa1-6, and 2.5×10^{6} CT2A tumor cells were injected subcutaneously into the right flank of mice. A total of 2×10^{6} E0771 tumor cells were injected into mouse breast pads. The length (L), width (W), and height (H) of the tumors of mice were recorded starting at day 6. The tumor volume (V) was calculated using the formula $V\ (\mathrm{mm}^3) = L\ (\mathrm{mm}) \times W\ (\mathrm{mm}) \times H\ (\mathrm{mm}) \times 0.5$. When tumors reached 1000 mm^3, mice were generally euthanized and recorded as dead for survival observation. For Hepa1-6 rechallenge tumor model, tumor-free mice were rechallenged with triple tumor cells 60 days after the first injection.

For depletion of immune cells, 100 μg of anti-mouse CD4 (BioXCell, GK1.5) and anti-mouse CD8α (BioXCell, 2.43) antibodies were delivered by intraperitoneal injection every week; 200 μg of anti-mouse CSF1R (BioXCell, AFS98) antibodies were injected every 5 days from day 11. For combined therapy, when the tumor volume reached 100 mm^3, mice were injected intraperitoneally four times with anti-mouse PD-L1 (BioXCell, 10F.9G2) antibodies at a dosage of 50 μg per mouse every 3 days.

Preparation of single-cell suspension for mouse samples

To obtain tumor-filtrating immune cells, tumors were sliced into small pieces of 1 to 2 mm in petri dishes and then digested in digestion buffer [10 mM Hepes, collagenase D (1.25 mg/ml), collagenase V (0.85 mg/ml), deoxyribonuclease I (30 U/ml), dispase II (1 mg/ml), and 10% FBS diluted in Hanks' balanced salt solution] for 45 min on a rotor at 37°C. The dissociated cells were passed through 70- and 40-μm cell strainers (BD) sequentially, centrifuged at 600*g* for 5 min at 4°C, and then prepared as single-cell suspension. Tumor-infiltrating immune cells were enriched from tumor tissues by magnetic separation using mouse CD45 MicroBeads (Miltenyi Biotec, catalog. no. 130-052-301).

Preparation of the tumor interstitial fluids

The preparation process for tumor interstitial fluid is as follows: Isolate tumor tissue and put it in an Eppendorf tube. Add an appropriate volume of PBS at a ratio of 1 ml of PBS per gram of tumor tissue. Use a tissue grinder to homogenize the tumor tissue. After grinding, centrifuge at 5000 rpm for 5 to 10 min and collect the supernatant, completing the preparation of the tumor interstitial fluid.

Flow cytometry

Anti-mouse CD16/32 and mouse immunoglobulin G2a antibodies were used to block nonspecific binding with Fc receptors before all surface staining. For staining, cells were stained with antibodies in PBS containing 2% FBS at 4°C for 30 min. The antibodies used for fluorescence-activated cell sorting (FACS) analyses are listed in table S9. The experimental operation followed the standard operating procedure for the CytoFLEX analyzer (Beckman Coulter), and FlowJo software was used for data analysis.

Immunohistochemistry

The tumor tissues were fixed with 4% formaldehyde and stained with H&E at the Servicebio company. Then, the infiltration of $CD4^+$ or $CD8^+$ T cells was visualized by immunohistochemical staining and calculated with a 5× objective using ImageJ software.

Intracellular cytokine staining

After surface staining, cells were washed by PBS and fixed with 100 μl of intracellular fixation buffer for 30 min at room temperature in the dark, followed by permeabilization of the cell membrane with 300 μl of permeabilization buffer. Last, cells were stained with antibodies against specific intracellular markers. The antibodies used for FACS analysis are listed in table S9.

T cell function assay

For T cell activation assay, T cells were enriched from the spleens with EasySep Mouse T cell isolation kit (STEMCELL) according to the manufacturer's instructions. Before the activation, anti-CD3ε (1 μg/ml) antibodies were precoated into the plate at 4°C for 12 hours. The anti-CD3ε antibodies and anti-CD28 (1 μg/ml) antibodies were used to stimulate T cells. After stimulation for 48 hours, the activation of T cells was detected by CytoFLEX analyzer (Beckman Coulter).

For T cell proliferation assay, OT-I T cells were enriched from the spleens of OT-I mice with EasySep Mouse $CD8^+$ T cell isolation kit (STEMCELL) according to the manufacturer's instructions. A total of 1×10^5 BMDMs were seeded in 24-well flat-bottom plates overnight. Before cocultured with 5×10^5 carboxyfluorescein diacetate succinimidyl ester (CFSE)–labeled OT-I T cells, BMDMs were cultured by purified OVA peptide (1 μg/ml) for 6 hours. After incubation for 48 hours, CFSE intensity was quantified by CytoFLEX analyzer (Beckman Coulter).

For TIL reactivation assay, tumor-infiltrating $CD4^+$ and $CD8^+$ T cells were enriched from the tumor tissues by magnetic separation using mouse $CD4^+$/$CD8^+$ (TIL) MicroBeads (Miltenyi Biotec, catalog. no. 130-116-480). TILs were reactivated by phorbol 12-myristate 13-acetate 9 (20 ng/ml) and ionomycin (1 μg/ml) for 6 hours. Then, the activation of TILs was detected by CytoFLEX analyzer (Beckman Coulter).

T cell adoptive transfer assay

Park2$^{-/-}$ and WT splenic $CD8^+$ T cells were isolated and cultured as described above. *Rag1*$^{-/-}$ mice were subcutaneously inoculated with 2×10^5 MC38 cells. Then, *Rag1*$^{-/-}$ recipient mice were injected intravenously with *Park2*$^{-/-}$ and WT splenic $CD8^+$ T cells on day 1. Tumor volume was supervised every 2 days starting at day 6.

Macrophage adoptive transfer assay

Park2$^{-/-}$ and WT BMDMs were prepared as previously described and digested into single cells. Hepa1-6 tumor–bearing WT mice were injected with *Park2*$^{-/-}$ and WT BMDMs (3×10^6 per mouse) intravenously on days 3, 6, and 9 after tumor inoculation. Tumor volume was supervised every 2 days starting at day 6.

In vitro phagocytosis assay

Phagocytosis assays were performed according to the previous studies (*53*, *54*). A total of 5×10^4 *Park2*$^{-/-}$ and WT BMDMs were seeded overnight in a 24-well tissue culture plate, treated or not treated with polyinosinic-polycytidylic acid (10 μg/ml), lipopolysaccharide (100 ng/ml), and IL-6 (100 ng/ml) for 24 hours. On the next day, 2×10^5 L1210 cells were labeled with 2.5 μM CFSE (Thermo Fisher Scientific) and incubated with *Park2*$^{-/-}$ and WT macrophages in non-FBS medium plus anti-mouse CD47 monoclonal antibody (10 μg/ml) or control immunoglobulin G for 2 hours at 37°C. After incubation, macrophages were washed four times using PBS and imaged with an inverted microscope. The phagocytosis efficiency was calculated as equation = (the number of macrophages containing $CFSE^+$ target cells) / total macrophages × 100.

DNA constructs and retroviral infection

To construct a series of Parkin variants, the full-length, point mutations S65A, S108A, and C430S of Parkin were cloned and fused to pMXs–green fluorescent protein (GFP), a retroviral vector. Raw264.7 cell lines were respectively infected with these plasmids pMXs-GFP using Lipofectamine 3000 and sorted according to comparable GFP expression. Primers were designed for polymerase chain reaction amplification and sanger sequencing of Parkin full-length, point mutations S65A, S108A, and C430S variants (forward, 5′-TCAAGGAGGACGGCAACATC-3′; reverse, 5′-CATCTGTTCTTGGCCCTGAG-3′). Detailed information about the construction strategies is provided in table S8.

Western blot

Cells were lysed in radioimmunoprecipitation assay lysis buffer (Beyotime Biotechnology, P0013B). Protein concentration was assessed using the bicinchoninic acid protein assay kit (Beyotime Biotechnology, P0012S). Samples were resolved using 10% polyacrylamide gel and transferred to polyvinylidene difluoride membranes. Membranes were blocked with 5% bovine serum albumin/Tris-buffered saline with 0.1% Tween 20 detergent for 1 hour at room temperature and incubated overnight at 4°C with antibodies recognizing MHC-I (ABclonal, A1013), Parkin (Santa Cruz Biotechnology, sc-32282), and ATG5 (Cell Signaling Technology, 12994T). Membranes were then probed with horseradish peroxidase–linked secondary antibodies and developed Pierce ECL Protein Blotting substrate (Thermo Fisher Scientific) using ChemiDoc XRS+ (Bio-Rad).

Enzyme-linked immunosorbent assay

Mouse IFN-γ (Servicebio, EK280/3-01) and IL-2 (Servicebio, EK202/2-01) enzyme-linked immunosorbent assay kits were used to determine the concentrations of IFN-γ and IL-2 in tumor interstitial fluids following standard protocols.

scRNA-seq data processing and analysis

Cell Ranger 5.0.1 (10x Genomics) was applied to align the gene expression libraries to the mm10 genome and generate gene-cell count matrices using default parameters. Then, the initial expression matrices were further filtered by Seurat 3.15 R package (*55*) according to the following criteria: (i) Cells that contained less than 500 molecular identifiers were filtered out; (ii) cells with less than 200 or more than 6000 genes were removed; (iii) cells were excluded if contained higher than 15% mitochondrial counts or lower than 20% ribosomal counts; (iv) genes present in less than four cells were precluded; and (v) DoubletFinder 2.03 in R (*56*) was used to exclude 2.5% potential doublets. In the end, a total of 40,119 cells with 22,620 genes were retained for the downstream analyses.

Seurat was subsequently used to normalize the raw expression matrix, find highly variable features, identify integration anchors, integrate samples, and scale features. Principal components analysis was performed on the 2000 most highly variable features to project into the top 20 principal components, and dimension reduction was conducted via Uniform Manifold Approximation and Projection (UMAP) or t-SNE. Samples were further clustered by shared nearest neighbor–based Louvain algorithm as implemented in function FindClusters of Seurat. Cell clusters were annotated by the expression of known immune cell markers, including *Cd3d*, *Cd3e*, *Cd3g*, *Cd28* (T cells), *Cd8a*, *Cd8b* ($CD8^+$ T cells), *Cd4*, *Il7r*, *Ctla4* ($CD4^+$ T cells), *Foxp3*, *Il2ra*, *Il2rb*, *Pdcd1* (T_{regs}), *Cd14*, *Sell* (monocytes), *Fcgr3*, *Adgre1*, *Itgam*, *Cd68*, *Cd163*, *Csf1r* (macrophages), *Itgax*, *Flt3*, *Batf*, *Thbd*, *Clec9a* (dendritic cells), *Tpsab1*, *Kit*, *Enpp3*, *Tpsb2* (mast cells), *Fut4*, *Csf3r*, *Cxcr2*, *S100a8*, *S100a9* (neutrophils), *Nkg7*, *Ccl5*, *Ncr1*, *Klrc1*, *Klrk1* (NK cells), *Cd19*, *Ms4a1*, *Cd79a*, *Cd79b*, and *Blnk* (B cells).

Differential expression and pathway activity analyses

DEGs were identified via Wilcoxon test of FindMarkers and FindAllMarkers functions embedded in Seurat with a $\log_2$FC threshold of 0.25 and adjusted $P \leq 0.05$. GO and KEGG analyses were conducted by clusterProfiler 4.05 R package (*57*) based on the DEGs of each cell cluster. Gene set variation analysis 1.40.1 package in R (*58*) with default setting was implemented in ssGSEAs to assign normalized enrichment score for individual cells.

Gene signatures

The difference in signature scores between WT and *Park2*$^{-/-}$ $CD8^+$ T cells was evaluated using Wilcoxon rank-sum test, visualized by violin, circle, or empirical cumulative distribution function (ECDF) plots. Detailed information about the gene signatures is provided in table S1.

Developmental trajectory inference

Monocle 2.20.0 in R 28825705 was used to infer T cell trajectories, and dimensionality reduction and cell ordering were performed with default settings. The progenitor signature scores of all T cells were generated by ssGSEA to identify innate cell clusters, also considered the start of the pseudotime trajectory. Exhaustion and inhibitory scores for each T cells were added to Monocle and Seurat to produce further trajectory and ridge plots, respectively.

Determining potential ligand-receptor interactions

R package CellChat 1.1.3 (*59*) was used to study and visualize the communicating interactions between T cell and myeloid cell clusters, selecting the cell-cell contacts and mouse protein-protein interactions. To infer the up-regulated ligand-receptor pairs, the interactions of WT and *Park2*$^{-/-}$ group populations were compared (table S4). Public ligand-receptor repository CellPhoneDB 2.1.1 (*60*) was then applied to complement the cell-cell communications between $CD8^+$ T cell and macrophage subclusters (table S5).

TCR-seq data processing and analysis

TCR-seq was conducted by Illumina HiSeq system (PE150 mode) using ImmuHub TCR profiling system (ImmuQuad Biotech). The V, D, J, and C segments were aligned with the international immunogenetic database to identify nucleotide and amino acid sequences of TCRα/β complementarity-determining region 3, excluding out-of-frame and stop codon sequences. The amounts of TCRα/β clonotype were determined by the adding numbers of each clone sharing the same nucleotide sequence of complementarity-determining region 3. The characteristics of the TCRα clonotypes were displayed in table S6.

Immune cell infiltration and correlation analysis

The infiltration levels of immune cells were calculated as normalized enrichment score from TCGA pan-cancer RNA-seq data (*61*) based on cell markers extracted from The Cancer Immunome Atlas (*62*). Effector memory $CD8^+$ T cell scores were afterward analyzed for their correlation with the expression level of *PARK2* in pan-cancer.

Assessment of predictive response efficacy for ICB responses

Two ICB cohorts were collected to compare the expression level of *PARK2* between responders (complete response or partial response) and nonresponders (stable disease or progressive disease) to ICBs. IMvigor210 dataset containing patients with mUC treated with PD-L1 inhibitors and Mariathasan *et al.* (*63*) cohort with patients with melanoma receiving anti–CTLA-4 (Cytotoxic T-Lymphocyte Associated Protein 4) treatment (*64*) were enrolled.

Survival analysis with the *Park2*$^{-/-}$signature in pan-cancer

The *Park2*$^{-/-}$ signature lists were defined as the intersect top 20 up-regulated DEGs in KO group of the cluster macro_CD80 and macro_C1qc. *Park2*$^{-/-}$ scores were first calculated as the sum TPM (transcripts per million, transcripts per kilobase of exon model per million mapped reads) value based on expression profiles from the TCGA (*61*). The *Park2*$^{-/-}$ signature gene lists and the computed scores were described in table S7. Pan-cancer survival Kaplan-Meier survival curves were plotted by survival 3.2-13 package in R, with the best divisions of *PARK2* expression level separately counted by R survminer 0.49 package, and the cutoff for the survival analysis was median.

Statistical analysis

All statistical analyses were conducted by GraphPad Prism 8.21 or R 4.03 for evaluating statistical significance or plotting. Comparisons between two groups were computed by two-tailed paired or unpaired *t* test, and two-way analysis of variance (ANOVA) test was applied in comparisons with more than two groups. Correlation was assessed by Spearman or Pearson test, and cumulative survival was analyzed by log-rank test. *P* values were corrected by Benjamini-Hochberg method in multiple tests, and $P \leq 0.05$ was considered significant for all statistical analyses.

Supplementary Materials

The PDF file includes:
Figs. S1 to S13
Legends for data S1 to S9

Other Supplementary Material for this manuscript includes the following:
Data S1 to S9

REFERENCES AND NOTES

1. L. Gandhi, D. Rodriguez-Abreu, S. Gadgeel, E. Esteban, E. Felip, F. De Angelis, M. Domine, P. Clingan, M. J. Hochmair, S. F. Powell, S. Y.-S. Cheng, H. G. Bischoff, N. Peled, F. Grossi, R. R. Jennens, M. Reck, R. Hui, E. B. Garon, M. Boyer, B. Rubio-Viqueira, S. Novello, T. Kurata, J. E. Gray, J. Vida, Z. Wei, J. Yang, H. Raftopoulos, M. C. Pietanza, M. C. Garassino, KEYNOTE-189 Investigators, Pembrolizumab plus chemotherapy in metastatic non–small-cell lung cancer. *N. Engl. J. Med.* **378**, 2078–2092 (2018).
2. R. J. Motzer, B. Escudier, D. F. McDermott, S. George, H. J. Hammers, S. Srinivas, S. S. Tykodi, J. A. Sosman, G. Procopio, E. R. Plimack, D. Castellano, T. K. Choueiri, H. Gurney, F. Donskov, P. Bono, J. Wagstaff, T. C. Gauler, T. Ueda, Y. Tomita, F. A. Schutz, C. Kollmannsberger, J. Larkin, A. Ravaud, J. S. Simon, L.-A. Xu, I. M. Waxman, P. Sharma, CheckMate 025 Investigators, Nivolumab versus everolimus in advanced renal-cell carcinoma. *N. Engl. J. Med.* **373**, 1803–1813 (2015).
3. P. Schmid, S. Adams, H. S. Rugo, A. Schneeweiss, C. H. Barrios, H. Iwata, V. Dieras, R. Hegg, S. A. Im, G. Shaw Wright, V. Henschel, L. Molinero, S. Y. Chui, R. Funke, A. Husain, E. P. Winer, S. Loi, L. A. Emens, IMpassion130 Trial Investigators, Atezolizumab and nab-paclitaxel in advanced triple-negative breast cancer. *N. Engl. J. Med.* **379**, 2108–2121 (2018).
4. X. Yang, R. Yin, L. Xu, Neoadjuvant PD-1 blockade in resectable lung cancer. *N. Engl. J. Med.* **379**, e14 (2018).
5. P. Sharma, S. Hu-Lieskovan, J. A. Wargo, A. Ribas, Primary, adaptive, and acquired resistance to cancer immunotherapy. *Cell* **168**, 707–723 (2017).
6. G. Morad, B. A. Helmink, P. Sharma, J. A. Wargo, Hallmarks of response, resistance, and toxicity to immune checkpoint blockade. *Cell* **184**, 5309–5337 (2021).
7. M. A. Stanczak, N. R. Mantuano, N. Kirchhammer, D. E. Sanin, F. Jacob, R. Coelh, A. V. Everest-Dass, J. Wang, M. P. Trefny, G. Monaco, A. Bärenwaldt, M. A. Gray, A. Petrone, A. S. Kashyap, K. Glatz, B. Kasenda, K. Normington, J. Broderick, L. Peng, O. M. T. Pearce, E. L. Pearce, C. R. Bertozzi, A. Zippelius, H. Läubli, Targeting cancer glycosylation repolarizes tumor-associated macrophages allowing effective immunecheckpoint blockade. *Sci. Transl. Med.* **14**, eabj1270 (2022).
8. A. J. M. Howden, J. L. Hukelmann, A. Brenes, L. Spinelli, L. V. Sinclair, A. I. Lamond, D. A. Cantrell, Quantitative analysis of T cell proteomes and environmental sensors during T cell differentiation. *Nat. Immunol.* **20**, 1542–1554 (2019).
9. B. Liu, X. Hu, K. Feng, R. Gao, Z. Xue, S. Zhang, Y. Zhang, E. Corse, Y. Hu, W. Han, Z. Zhang, Temporal single-cell tracing reveals clonal revival and expansion of precursor exhausted T cells during anti-PD-1 therapy in lung cancer. *Nat. Cancer* **3**, 108–121 (2022).
10. Y. Mei, X. Wang, J. Zhang, D. Liu, J. He, C. Huang, J. Liao, Y. Wang, Y. Feng, H. Li, X. Liu, L. Chen, W. Yi, X. Chen, H. M. Bai, X. Wang, Y. Li, L. Wang, Z. Liang, X. Ren, L. Qiu, Y. Hui, Q. Zhang, Q. Leng, J. Chen, G. Jia, Siglec-9 acts as an immune-checkpoint molecule on macrophages in glioblastoma, restricting T-cell priming and immunotherapy response. *Nat. Cancer* **4**, 1273–1291 (2023).
11. T. Baumann, A. Dunkel, C. Schmid, S. Schmitt, M. Hiltensperger, K. Lohr, V. Laketa, S. Donakonda, U. Ahting, B. Lorenz-Depiereux, J. E. Heil, J. Schredelseker, L. Simeoni, C. Fecher, N. Korber, T. Bauer, N. Huser, D. Hartmann, M. Laschinger, K. Eyerich, S. Eyerich, M. Anton, M. Streeter, T. Wang, B. Schraven, D. Spiegel, F. Assaad, T. Misgeld, H. Zischka, P. J. Murray, A. Heine, M. Heikenwalder, T. Korn, C. Dawid, T. Hofmann, P. A. Knolle, B. Hochst, Regulatory myeloid cells paralyze T cells through cell-cell transfer of the metabolite methylglyoxal. *Nat. Immunol.* **21**, 555–566 (2020).
12. B. G. Nixon, F. Kuo, L. Ji, M. Liu, K. Capistrano, M. Do, R. A. Franklin, X. Wu, E. R. Kansler, R. M. Srivastava, T. A. Purohit, A. Sanchez, L. Vuong, C. Krishna, X. Wang, H. C. Morse III, J. J. Hsieh, T. A. Chan, K. M. Murphy, J. J. Moon, A. A. Hakimi, M. O. Li, Tumor-associated macrophages expressing the transcription factor IRF8 promote T cell exhaustion in cancer. *Immunity* **55**, 2044–2058.e5 (2022).
13. S. Ma, B. Sun, S. Duan, J. Han, T. Barr, J. Zhang, M. B. Bissonnette, M. Kortylewski, C. He, J. Chen, M. A. Caligiuri, J. Yu, YTHDF2 orchestrates tumor-associated macrophage reprogramming and controls antitumor immunity through CD8$^+$ T cells. *Nat. Immunol.* **24**, 255–266 (2023).
14. D. G. DeNardo, B. Ruffell, Macrophages as regulators of tumour immunity and immunotherapy. *Nat. Rev. Immunol.* **19**, 369–382 (2019).
15. L. Cassetta, J. W. Pollard, A timeline of tumour-associated macrophage biology. *Nat. Rev. Cancer* **23**, 238–257 (2023).
16. M. Binnewies, E. W. Roberts, K. Kersten, V. Chan, D. F. Fearon, M. Merad, L. M. Coussens, D. I. Gabrilovich, S. Ostrand-Rosenberg, C. C. Hedrick, R. H. Vonderheide, M. J. Pittet, R. K. Jain, W. Zou, T. K. Howcroft, E. C. Woodhouse, R. A. Weinberg, M. F. Krummel, Understanding the tumor immune microenvironment (TIME) for effective therapy. *Nat. Med.* **24**, 541–550 (2018).
17. L. Keren, M. Bosse, D. Marquez, R. Angoshtari, S. Jain, S. Varma, S. R. Yang, A. Kurian, D. Van Valen, R. West, S. C. Bendall, M. Angelo, A structured tumor-immune microenvironment in triple negative breast cancer revealed by multiplexed ion beam imaging. *Cell* **174**, 1373–1387.e19 (2018).
18. J.-F. Trempe, V. Sauve, K. Grenier, M. Seirafi, M. Y. Tang, M. Menade, S. Al-Abdul-Wahid, J. Krett, K. Wong, G. Kozlov, B. Nagar, E. A. Fon, K. Gehring, Structure of parkin reveals mechanisms for ubiquitin ligase activation. *Science* **340**, 1451–1455 (2013).
19. C. Arkinson, H. Walden, Parkin function in Parkinson's disease. *Science* **360**, 267–268 (2018).
20. F. Koyano, K. Okatsu, H. Kosako, Y. Tamura, E. Go, M. Kimura, Y. Kimura, H. Tsuchiya, H. Yoshihara, T. Hirokawa, T. Endo, E. A. Fon, J. F. Trempe, Y. Saeki, K. Tanaka, N. Matsuda, Ubiquitin is phosphorylated by PINK1 to activate parkin. *Nature* **510**, 162–166 (2014).
21. T. Wauer, M. Simicek, A. Schubert, D. Komander, Mechanism of phospho-ubiquitin-induced PARKIN activation. *Nature* **524**, 370–374 (2015).
22. M. Reale, C. Iarlori, A. Thomas, D. Gambi, B. Perfetti, M. Di Nicola, M. Onofrj, Peripheral cytokines profile in Parkinson's disease. *Brain Behav. Immun.* **23**, 55–63 (2009).
23. D. A. Sliter, J. Martinez, L. Hao, X. Chen, N. Sun, T. D. Fischer, J. L. Burman, Y. Li, Z. Zhang, D. P. Narendra, H. Cai, M. Borsche, C. Klein, R. J. Youle, Parkin and PINK1 mitigate STING-induced inflammation. *Nature* **561**, 258–262 (2018).
24. S. B. Lee, J. J. Kim, S. A. Han, Y. Fan, L. S. Guo, K. Aziz, S. Nowsheen, S. S. Kim, S. Y. Park, Q. Luo, J. O. Chung, S. I. Choi, A. Aziz, P. Yin, S. Y. Tong, F. C. Fiesel, W. Springer, J. S. Zhang, Z. Lou, The AMPK-Parkin axis negatively regulates necroptosis and tumorigenesis by inhibiting the necrosome. *Nat. Cell Biol.* **21**, 940–951 (2019).
25. C.-M. Hung, P. S. Lombardo, N. Malik, S. N. Brun, K. Hellberg, J. L. Van Nostrand, D. Garcia, J. Baumgart, K. Diffenderfer, J. M. Asara, R. J. Shaw, AMPK/ULK1-mediated phosphorylation of Parkin ACT domain mediates an early step in mitophagy. *Sci. Adv.* **7**, eabg4544 (2021).
26. D. Matheoud, A. Sugiura, A. Bellemare-Pelletier, A. Laplante, C. Rondeau, M. Chemali, A. Fazel, J. J. Bergeron, L. E. Trudeau, Y. Burelle, E. Gagnon, H. M. McBride, M. Desjardins, Parkinson's disease-related proteins PINK1 and Parkin repress mitochondrial antigen presentation. *Cell* **166**, 314–327 (2016).
27. C. Li, Y. Zhang, X. Cheng, H. Yuan, S. Zhu, J. Liu, Q. Wen, Y. Xie, J. Liu, G. Kroemer, D. J. Klionsky, M. T. Lotze, H. J. Zeh, R. Kang, D. Tang, PINK1 and PARK2 suppress pancreatic tumorigenesis through control of mitochondrial iron-mediated immunometabolism. *Dev. Cell* **46**, 441–455.e8 (2018).
28. J. Liu, C. Zhang, H. Wu, X. X. Sun, Y. Li, S. Huang, X. Yue, S. E. Lu, Z. Shen, X. Su, E. White, B. G. Haffty, W. Hu, Z. Feng, Parkin ubiquitinates phosphoglycerate dehydrogenase to suppress serine synthesis and tumor progression. *J. Clin. Invest.* **130**, 3253–3269 (2020).
29. C. Zhang, M. Lin, R. Wu, X. Wang, B. Yang, A. J. Levine, W. Hu, Z. Feng, Parkin, Parkin, a p53 target gene, mediates the role of p53 in glucose metabolism and the Warburg effect. *Proc. Natl. Acad. Sci. U.S.A.* **108**, 16259–16264 (2011).
30. Y. R. Yu, H. Imrichova, H. Wang, T. Chao, Z. Xiao, M. Gao, M. Rincon-Restrepo, F. Franco, R. Genolet, W. C. Cheng, C. Jandus, G. Coukos, Y. F. Jiang, J. W. Locasale, A. Zippelius, P. S. Liu, L. Tang, C. Bock, N. Vannini, P. C. Ho, Disturbed mitochondrial dynamics in CD8$^+$ TILs reinforce T cell exhaustion. *Nat. Immunol.* **21**, 1540–1551 (2020).
31. D. Vijayan, A. Young, M. W. L. Teng, M. J. Smyth, Targeting immunosuppressive adenosine in cancer. *Nat. Rev. Cancer* **17**, 709–724 (2017).
32. H. Zhao, L. Wu, G. Yan, Y. Chen, M. Zhou, Y. Wu, Y. Li, Inflammation and tumor progression: Signaling pathways and targeted intervention. *Signal Transduct. Target. Ther.* **6**, 263 (2021).
33. M. Barry, R. C. Bleackley, Cytotoxic T lymphocytes: All roads lead to death. *Nat. Rev. Immunol.* **2**, 401–409 (2002).
34. Y. Zhang, Z. Zhang, The history and advances in cancer immunotherapy: Understanding the characteristics of tumor-infiltrating immune cells and their therapeutic implications. *Cell. Mol. Immunol.* **17**, 807–821 (2020).
35. K. Nakamura, M. J. Smyth, Myeloid immunosuppression and immune checkpoints in the tumor microenvironment. *Cell. Mol. Immunol.* **17**, 1–12 (2020).
36. L. Zhang, Z. Li, K. M. Skrzypczynska, Q. Fang, W. Zhang, S. A. O'Brien, Y. He, L. Wang, Q. Zhang, A. Kim, R. Gao, J. Orf, T. Wang, D. Sawant, J. Kang, D. Bhatt, D. Lu, C.-M. Li,

A. S. Rapaport, K. Perez, Y. Ye, S. Wang, X. Hu, X. Ren, W. Ouyang, Z. Shen, J. G. Egen, Z. Zhang, X. Yu, Single-cell analyses inform mechanisms of myeloid-targeted therapies in colon cancer. *Cell* **181**, 442–459.e29 (2020).

37. C. A. Bernhard, C. Ried, S. Kochanek, T. Brocker, CD169$^+$ macrophages are sufficient for priming of CTLs with specificities left out by cross-priming dendritic cells. *Proc. Natl. Acad. Sci. U.S.A.* **112**, 5461–5466 (2015).
38. T. L. Tang-Huau, P. Gueguen, C. Goudot, M. Durand, M. Bohec, S. Baulande, B. Pasquier, S. Amigorena, E. Segura, Human in vivo-generated monocyte-derived dendritic cells and macrophages cross-present antigens through a vacuolar pathway. *Nat. Commun.* **9**, 2570 (2018).
39. D. Xia, S. Hao, J. Xiang, CD8$^+$ cytotoxic T-APC stimulate central memory CD8$^+$ T cell responses via acquired peptide-MHC class I complexes and CD80 costimulation, and IL-2 secretion. *J. Immunol.* **177**, 2976–2984 (2006).
40. D. F. Egan, D. B. Shackelford, M. M. Mihaylova, S. Gelino, R. A. Kohnz, W. Mair, D. S. Vasquez, A. Joshi, D. M. Gwinn, R. Taylor, J. M. Asara, J. Fitzpatrick, A. Dillin, B. Viollet, M. Kundu, M. Hansen, R. J. Shaw, Phosphorylation of ULK1 (hATG1) by AMP-activated protein kinase connects energy sensing to mitophagy. *Science* **331**, 456–461 (2011).
41. J. Kim, M. Kundu, B. Viollet, K. L. Guan, AMPK and mTOR regulate autophagy through direct phosphorylation of Ulk1. *Nat. Cell Biol.* **13**, 132–141 (2011).
42. K. Yamamoto, A. Venida, J. Yano, D. E. Biancur, M. Kakiuchi, S. Gupta, A. S. W. Sohn, S. Mukhopadhyay, E. Y. Lin, S. J. Parker, R. S. Banh, J. A. Paulo, K. W. Wen, J. Debnath, G. E. Kim, J. D. Mancias, D. T. Fearon, R. M. Perera, A. C. Kimmelman, Autophagy promotes immune evasion of pancreatic cancer by degrading MHC-I. *Nature* **581**, 100–105 (2020).
43. A. D. Waldman, J. M. Fritz, M. J. Lenardo, A guide to cancer immunotherapy: From T cell basic science to clinical practice. *Nat. Rev. Immunol.* **20**, 651–668 (2020).
44. M. F. Sanmamed, L. Chen, A paradigm shift in cancer immunotherapy: From enhancement to normalization. *Cell* **175**, 313–326 (2018).
45. M. Klichinsky, M. Ruella, O. Shestova, X. M. Lu, A. Best, M. Zeeman, M. Schmierer, K. Gabrusiewicz, N. R. Anderson, N. E. Petty, K. D. Cummins, F. Shen, X. Shan, K. Veliz, K. Blouch, Y. Yashiro-Ohtani, S. S. Kenderian, M. Y. Kim, R. S. O'Connor, S. R. Wallace, M. S. Kozlowski, D. M. Marchione, M. Shestov, B. A. Garcia, C. H. June, S. Gill, Human chimeric antigen receptor macrophages for cancer immunotherapy. *Nat. Biotechnol.* **38**, 947–953 (2020).
46. A. Mantovani, F. Marchesi, A. Malesci, L. Laghi, P. Allavena, Tumour-associated macrophages as treatment targets in oncology. *Nat. Rev. Clin. Oncol.* **14**, 399–416 (2017).
47. S. Jhunjhunwala, C. Hammer, L. Delamarre, Antigen presentation in cancer: Insights into tumour immunogenicity and immune evasion. *Nat. Rev. Cancer* **21**, 298–312 (2021).
48. C. Cebrian, F. A. Zucca, P. Mauri, J. A. Steinbeck, L. Studer, C. R. Scherzer, E. Kanter, S. Budhu, J. Mandelbaum, J. P. Vonsattel, L. Zecca, J. D. Loike, D. Sulzer, MHC-I expression renders catecholaminergic neurons susceptible to T-cell-mediated degeneration. *Nat. Commun.* **5**, 3633 (2014).
49. D. R. Wang, X. L. Wu, Y. L. Sun, Therapeutic targets and biomarkers of tumor immunotherapy: Response versus non-response. *Signal Transduct. Target. Ther.* **7**, 331 (2022).
50. K. Pan, H. Farrukh, V. Chittepu, H. Xu, C. X. Pan, Z. Zhu, CAR race to cancer immunotherapy: From CAR T, CAR NK to CAR macrophage therapy. *J. Exp. Clin. Cancer Res.* **41**, 119 (2022).
51. J. Chen, M. C. Zhong, H. Guo, D. Davidson, S. Mishel, Y. Lu, I. Rhee, L. A. Perez-Quintero, S. Zhang, M. E. Cruz-Munoz, N. Wu, D. C. Vinh, M. Sinha, V. Calderon, C. A. Lowell, J. S. Danska, A. Veillette, SLAMF7 is critical for phagocytosis of haematopoietic tumour cells via Mac-1 integrin. *Nature* **544**, 493–497 (2017).
52. Z. Tang, D. Davidson, R. Li, M. C. Zhong, J. Qian, J. Chen, A. Veillette, Inflammatory macrophages exploit unconventional pro-phagocytic integrins for phagocytosis and anti-tumor immunity. *Cell Rep.* **37**, 110111 (2021).
53. C. Zhong, L. Wang, S. Hu, C. Huang, Z. Xia, J. Liao, W. Yi, J. Chen, Poly(I:C) enhances the efficacy of phagocytosis checkpoint blockade immunotherapy by inducing IL-6 production. *J. Leukoc. Biol.* **110**, 1197–1208 (2021).
54. Y. Y. Li, X. Y. Wang, Y. Li, X. M. Wang, J. Liao, Y. Z. Wang, H. Hong, W. Yi, J. Chen, Targeting CD43 optimizes cancer immunotherapy through reinvigorating antitumor immune response in colorectal cancer. *Cell. Oncol.* **46**, 777–791 (2023).
55. T. Stuart, A. Butler, P. Hoffman, C. Hafemeister, E. Papalexi, W. M. Mauck III, Y. Hao, M. Stoeckius, P. Smibert, R. Satija, Comprehensive integration of single-cell data. *Cell* **177**, 1888–1902.e21 (2019).
56. C. S. McGinnis, L. M. Murrow, Z. J. Gartner, DoubletFinder: Doublet detection in single-cell RNA sequencing data using artificial nearest neighbors. *Cell Syst.* **8**, 329–337.E4 (2019).
57. G. Yu, L. G. Wang, Y. Han, Q. Y. He, clusterProfiler: An R package for comparing biological themes among gene clusters. *OMICS* **16**, 284–287 (2012).
58. S. Hänzelmann, R. Castelo, J. Guinney, GSVA: Gene set variation analysis for microarray and RNA-seq data. *BMC Bioinformatics* **14**, 7 (2013).
59. S. Jin, C. F. Guerrero-Juarez, L. Zhang, I. Chang, R. Ramos, C.-H. Kuan, P. Myung, M. V. Plikus, Q. Nie, Inference and analysis of cell-cell communication using CellChat. *Nat. Commun.* **12**, 1088 (2021).
60. M. Efremova, M. Vento-Tormo, S. A. Teichmann, R. Vento-Tormo, CellPhoneDB: Inferring cell-cell communication from combined expression of multi-subunit ligand-receptor complexes. *Nat. Protoc.* **15**, 1484–1506 (2020).
61. V. Thorsson, D. L. Gibbs, S. D. Brown, D. Wolf, D. S. Bortone, T. H. O. Yang, E. Porta-Pardo, G. F. Gao, C. L. Plaisier, J. A. Eddy, E. Ziv, A. C. Culhane, E. O. Paull, I. K. A. Sivakumar, A. J. Gentles, R. Malhotra, F. Farshidfar, A. Colaprico, J. S. Parker, L. E. Mose, N. S. Vo, J. Liu, Y. Liu, J. Rader, V. Dhankani, S. M. Reynolds, R. Bowlby, A. Califano, A. D. Cherniack, D. Anastassiou, D. Bedognetti, Y. Mokrab, A. M. Newman, A. Rao, K. Chen, A. Krasnitz, H. Hu, T. M. Malta, H. Noushmehr, C. S. Pedamallu, S. Bullman, A. I. Ojesina, A. Lamb, W. Zhou, H. Shen, T. K. Choueiri, J. N. Weinstein, J. Guinney, J. Saltz, R. A. Holt, C. S. Rabkin, A. J. Lazar, J. S. Serody, E. G. Demicco, M. L. Disis, B. G. Vincent, I. Shmulevich, The immune landscape of cancer. *Immunity* **48**, 812–830.E14 (2018).
62. P. Charoentong, F. Finotello, M. Angelova, C. Mayer, M. Efremova, D. Rieder, H. Hackl, Z. Trajanoski, Pan-cancer immunogenomic analyses reveal genotype-immunophenotype relationships and predictors of response to checkpoint blockade. *Cell Rep.* **18**, 248–262 (2017).
63. S. Mariathasan, S. J. Turley, D. Nickles, A. Castiglioni, K. Yuen, Y. Wang, E. E. Kadel III, H. Koeppen, J. L. Astarita, R. Cubas, S. Jhunjhunwala, R. Banchereau, Y. Yang, Y. Guan, C. Chalouni, J. Ziai, Y. Şenbabaoğlu, S. Santoro, D. Sheinson, J. Hung, J. M. Giltnane, A. A. Pierce, K. Mesh, S. Lianoglou, J. Riegler, R. A. D. Carano, P. Eriksson, M. Höglund, L. Somarriba, D. L. Halligan, M. S. van der Heijden, Y. Loriot, J. E. Rosenberg, L. Fong, I. Mellman, D. S. Chen, M. Green, C. Derleth, G. D. Fine, P. S. Hegde, R. Bourgon, T. Powles, TGFβ attenuates tumour response to PD-L1 blockade by contributing to exclusion of T cells. *Nature* **554**, 544–548 (2018).
64. E. M. Van Allen, D. Miao, B. Schilling, S. A. Shukla, C. Blank, L. Zimmer, A. Sucker, U. Hillen, M. H. G. Foppen, S. M. Goldinger, J. Utikal, J. C. Hassel, B. Weide, K. C. Kaehler, C. Loquai, P. Mohr, R. Gutzmer, R. Dummer, S. Gabriel, C. J. Wu, D. Schadendorf, L. A. Garraway, Genomic correlates of response to CTLA-4 blockade in metastatic melanoma. *Science* **350**, 207–211 (2015).

Acknowledgments: We thank Z. Yin (Jinan University) and W. Yang (Southern Medical University) for help and discussion. We would like to thank Guangdong Engineering & Technology Research Center for Disease-Model Animals, Laboratory Animal Center, Zhongshan School of Medicine for support in all animal experiments. **Funding:** This work was supported by National Key R&D Program of China (2020YFA0509400 and 2019YFA0110300 to J.C.), National Natural Science Foundation of China (82150117 and 82071745 to J.C. and 82101329 to W.Y.), Guangdong project (2019QN01Y212 to J.C.), Guangzhou Science and Technology Plan Project (202201011475 to W.Y.), and Guangdong Provincial Key Area R&D Program (2023B1111050004 to W.Y.). **Author contributions:** Xin. Wang, Yi. Li, and Ya. Li wrote the original manuscript. J.C., W.Y., and J.L. supervised the research and authored the final manuscript. Xin. Wang and Yi. Li conceived and conducted most experiments and data curation with the help of Xiu. Wang, H.S., J.L., and Y.W. Xin. Wang performed the scRNA-seq, and Ya. Li performed the bioinformatic analyses. C.H., C.M, L.W., and C.Z. helped with the animal experiments. Z.X., Y.F., Y.Liu, C.L., and W.M. assisted with the laboratory animals and scRNA-seq. L.Z., W.C., D.Y., J.O., H.H., and J.D. provided guidance for the mouse experiments and data analyses. E.A.F. and J.-F.T. contributed to the designing functional assays of Parkin mutants. All authors have reviewed and approved the manuscript. **Competing interests:** The authors declare that they have no competing interests. **Data and materials availability:** All data needed to evaluate the conclusions in the paper are present in the paper and/or the Supplementary Materials. The sequence data have been deposited in the Genome Sequence Archive in BIG Data Center under the accession code GSE241129.

Submitted 2 January 2024
Accepted 18 February 2025
Published 21 March 2025
10.1126/sciadv.adn8402